ABSTRACT

Title of Thesis:	COMPARISON OF HIGH STRAIN RATE PROPERTIES OF ADDITIVELY MANUFACTURED AND WROUGHT INCONEL 625 VIA KOLSKY BAR TESTING
	Jason Michael Morin, Master of Science, 2019
Thesis Directed By:	Professor William Fourney Mechanical and Aerospace Engineering

Additive manufacturing is becoming an important part of modern manufacturing technology. Before additively manufactured parts gain widespread adoption, the material properties of the additively manufactured material itself must be accurately quantified. Stress strain curves must be produced over a wide variety of test conditions so that accurate modeling of material behavior can be done. Materials that may undergo dynamic loading must therefore be tested under dynamic conditions. In this study the tensile and high strain rate compressive material properties of additively manufactured Inconel 625 are compared to conventionally formed wrought material. The results of testing showed that there is a clear difference in material properties between wrought and additively manufactured Inconel 625 in tension and compression. The additively manufactured tensile samples showed anisotropy between print directions of approximately ±10%. The printed samples had a 35% higher yield strength, a similar ultimate strength, and 20-40% the elongation when compared to wrought. There was also a significant difference in properties between the additive and wrought materials during the compressive tests. The additive material showed little anisotropy and had a 30% higher yield stress than wrought. Additionally, the additive material had a higher strain hardening rate than the wrought samples. No significant strain rate effects were noted.

COMPARISON OF HIGH STRAIN RATE PROPERTIES OF ADDITIVELY
MANUFACTURED AND WROUGHT INCONEL 625 VIA KOLSKY BAR
TESTING

by

Jason Michael Morin

Thesis submitted to the Faculty of the Graduate School of the
University of Maryland, College Park, in partial fulfillment
of the requirements for the degree of
Master of Science
2019

Advisory Committee:
 Professor William Fourney, Chair
 Professor Hugh Bruck
 Professor Teng Li

Acknowledgements

Table of Contents

List of Tables

List of Figures

List of Abbreviations

AM-   Additive manufacturing or additively manufactured
EDM- Electrical Discharge Machining
IN625- Inconel 625
LPBF- Laser powder bed fusion
SHPB- Split Hopkinson pressure bar
UTS- Ultimate Strength

Chapter 1: Introduction to the Kolsky Bar

Introduction to High Strain Rate Testing

Stress strain diagrams are a fundamental representation of how material behaves in response to an applied force. All solid materials undergo some dimensional change when a static load is applied to them, but whether or not that change is measurable, temporary, or permanent depends on the properties of the material and the magnitude and duration of the stress applied to the specimen. Duration of the stress is important when considering creep and is not considered further in this study. The foundation of undergraduate mechanics of materials education can be summed up nicely with Hooke's Law, shown in Equation 1, which relates stress, σ, to strain, ε, and the modulus of elasticity, E.

$$\sigma = \varepsilon E \tag{1}$$

However, this equation leaves out something that is intuitive from our childhood experiments with putty, strain rate. When putty is pulled slow, it stretches. When it is pulled fast, it breaks. Therefore, with the simplest of demonstrations, we can see that the rate of deformation can drastically affect the properties of the material. So, Hooke's Law isn't wrong, it just doesn't tell the whole story. The element of time is hidden within it and will be of great importance in this study. Another factor is not included in Hooke's Law, temperature of the specimen. Temperature is important factor because materials lose strength as the temperature is increased. Therefore a 2-dimensional stress strain curve from a textbook is actually a slice of a 4-dimensional

surface made up of stress, strain, strain rate, and temperature, with strain rate and temperature chosen at fixed values.

Looking back at my undergraduate mechanical of materials textbook, strain rate isn't even mentioned. All of the stress strain curves contained are quasi-static or pseudo-static curves. This means that the material was stretched or compressed very slowly, at strain rates from 0.0001 s^{-1} to 1 s^{-1} [1–3]. Material properties taken in this manner are very useful for the design of static structures such as buildings and bridges. However, life is not static and many of the things around us undergo dynamic loading, sometimes violently so. Buildings react dynamically to the force of the wind or to a shockwave from an explosion. Automobiles experience taps on their bumpers while parallel parking as well as violent impacts on the highways. Bridge columns support the weight of the overpass but also must withstand the impact of a vehicle or the swaying of the structure in the wind. Even a coffee cup will react dynamically when it is dropped to the floor. These examples highlight why understanding dynamic material properties is important, even in many seemingly static situations.

There are several methods of obtaining the strain rate properties for materials, each of which is used in a specific strain rate regime. The method discussed in this paper is the Split Hopkinson Pressure Bar or Kolsky Bar which operates in the 200 s^{-1} to $10,000$ s^{-1} range[2]. This is the strain rate regime for most collision induced strains such a baseball on a bat, a vehicle collision, or a projectile hitting a target such as a bullet, arrow, or cannon ball [3].

History

John Hopkinson conducted experiments in the late 1800's on the rupture of iron wires and was the first to experimentally demonstrate the propagation of stress waves through solids. His son, Bertram Hopkinson, built upon his father's work by creating a ballistic pendulum that was able to measure the pressure versus time curves for high velocity impacts, such as bullets and explosions [1,2]. Herbert (Harry) Kolsky built upon the work of the Hopkinsons and in 1949 he added a second bar to the Hopkinson bar to create the Kolsky bar. This configuration is sometimes referred to as a Split Hopkinson Pressure Bar (SHPB)[4,5]. With this device he was able to measure the dynamic compressive stress strain response of materials. The names Kolsky bar and (Split) Hopkinson bar are used almost interchangeably but will be referred to as Kolsky bar for the duration of this writing.

Equipment Description

The basic Kolsky bar setup is shown in Figure 1. A projectile, also called a striker, is fired via a gas gun into the end of the incident bar. This impact causes an elastic stress wave to propagate down the length of the incident bar. The elastic deformation of the bar caused by the passing stress wave is measured by the first strain gage. When the stress wave reaches the end of the incident bar touching the test specimen, due to a mismatch in mechanical impedance, part of the wave is reflected back down the incident bar and part is transmitted through the specimen into the transmission bar. As the reflected wave travels back towards the striker end of the incident bar it is again measured by the first strain gage. The stress wave that travels through the specimen into the transmission bar is measured by the second strain gage. The strain

gage signals are sent through an amplifier into a high-speed oscilloscope for recording. These signals can then be used to determine the stress strain behavior of the test specimen as described in a later section. Lastly, since the bars are mounted in low friction bearings the momentum trap serves to keep the transmission bar from sliding out of the apparatus.
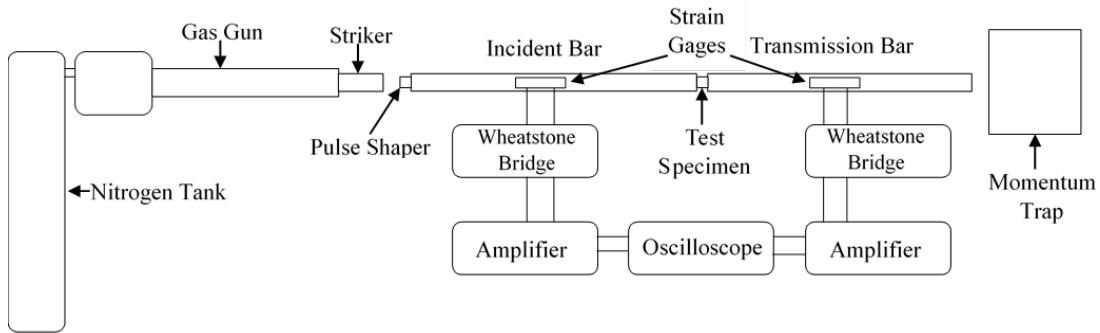
Figure 1. Kolsky Bar Setup

Strain Gage Theory

Strain gages are variable resistors that change resistance when elongated or shortened. In the context of the Kolsky bar, the change in length is caused by the passing compression wave. The ratio of change in resistance, ΔR, to the original resistance, R_0, is proportional to the change in length, ΔL, to the original length, L_0, as shown in Equation 2, where k is defined as the gage factor [2].

$$\frac{\Delta R}{R_0} = k \frac{\Delta L}{L_0} = k\varepsilon \qquad (2)$$

On both the incident bar and the transmission bar two strain gages are mounted directly across from each other. In this configuration axial strain will cause an equal deformation of each strain gage. If the bar experiences any bending one strain gage will elongate and one will shorten. When the gages are wired into a Wheatstone bridge the bending strain is cancelled out and the signal is reduced solely to axial

4

strain. A Wheatstone bridge is depicted in Figure 2. V_0 is the input voltage and ΔV is the output voltage. When $R_1 = R_2 = R_3 = R_4 = R$, $\Delta V = 0$.
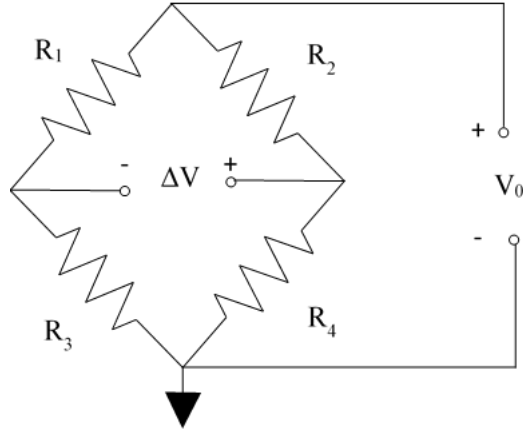
Figure 2. Wheatstone Bridge Circuit Diagram

The change in voltage across a Wheatstone bridge is shown in Equation 3.

$$\Delta V = V_0 \left(\frac{R_2}{R_2 + R_4} - \frac{R_1}{R_1 + R_3} \right) \tag{3}$$

In the Kolsky bar circuit R_2 and R_3 are strain gages and since they vary in resistance, they can be represented by $R_0 + \Delta R$, which is the original resistance plus the change in resistance. The resistors R_1 and R_4 do not undergo a change in resistance and are therefore represented by R_0. Substituting these into Equation 3 gives Equation 4, which simplifies to Equation 5.

$$\Delta V = V_0 \left(\frac{R_0 + \Delta R}{R_0 + \Delta R + R_0} - \frac{R_0}{R_0 + R_0 + \Delta R} \right) \tag{4}$$

$$\Delta V = V_0 \left(\frac{\Delta R}{2 R_0 + \Delta R} \right) \tag{5}$$

Rearranging Equation 2 gives Equation 6, which when substituted into Equation 5 becomes Equation 7:

$$\Delta R = k\varepsilon R_0 \tag{6}$$

$$\Delta V = V_0 \left(\frac{k\varepsilon R_0}{2\,R_0 + k\varepsilon R_0} \right) \tag{7}$$

Rearranged becomes:

$$\varepsilon = \frac{2\Delta V}{k(V_0 - \Delta V)} \tag{8}$$

This can be expressed as a multiplication of two fractions being:

$$\varepsilon = \frac{2\Delta V}{kV_0} \times \frac{1}{(1 - \frac{\Delta V}{V_0})} \tag{9}$$

When $\Delta V << V_0$ then the last term is ≈ 1 leaving:

$$\varepsilon = \frac{2\Delta V}{kV_0} \tag{10}$$

Since the change in voltage ΔV is amplified before reaching the oscilloscope, its value must be divided by the gain, G, which gives the final form of the equation relating the change in voltage to strain, Equation 11.

$$\varepsilon = \frac{2\Delta V}{GkV_0} \tag{11}$$

The next section will describe the mathematical theory which relates the strain gage measurements of the incident and transmission bar to the stress, strain, and strain rate of the test specimen in a Kolsky bar test.

Wave Theory

To relate the strain in the bars to the stress and strain experienced by the sample it is necessary to understand the propagation of 1-dimensional waves [2,3]. This is a well-

known equation in partial differential equation and is given by Equation 12. In the context of a Kolsky bar test, u is position and c is the elastic wave speed in the bars.

$$u_{xx} = \frac{1}{c^2} u_{tt} \tag{12}$$

This can also be represented by the d'Alembert formula, Equation 13, which represents the shapes and locations of a set of waves at any point in time. In the context of a Kolsky bar test these functions are the shapes and locations of the waves traveling in the incident bar at any point in time. The incident wave, denoted by the subscript i, travels through the incident bar from the striker end to the sample end and the reflected wave, denoted by subscript r, travels from the sample end to the striker end.

$$u = f(x - ct) + g(x + ct) = u_i + u_r \tag{13}$$

By definition 1-D strain is given by Equation 14:

$$\varepsilon = \frac{\delta u}{\delta x} \tag{14}$$

By differentiating Equation 13 with respect to x, the strain in the incident bar becomes:

$$\varepsilon = f' + g' = \varepsilon_i + \varepsilon_r \tag{15}$$

Differentiating Equation 13 with respect to time and combining it with Equation 15 gives the displacement rate for the incident bar, Equation 16.

$$\dot{u} = c(-f' + g') = c(-\varepsilon_i + \varepsilon_r) \tag{16}$$

There is a second d'Alembert equation that represents the wave in the transmission bar which is shown in Equation 17. However, this equation only has one term since

we are only interested in the transmitted wave traveling from the sample end to the momentum trap end, not its reflection.

$$u = h(x - ct) \tag{17}$$

Again, by differentiating with respect to x and time we find the strain and displacement rate equations for the transmitted bar, Equations 18 and 19 respectively.

$$\varepsilon = h' = \varepsilon_t \tag{18}$$

$$\dot{u} = -c\varepsilon_t \tag{19}$$

Strain in the sample is defined by Equation 20, where the subscripts 1 and 2 denote the position of the contact surface of the sample touching the incident and transmission bars respectively. The variable l_s is the length of the sample.

$$\varepsilon_s = \frac{u_1 - u_2}{l_s} \tag{20}$$

Differentiating with respect to time gives the strain rate of the sample:

$$\dot{\varepsilon}_s = \frac{\dot{u}_1 - \dot{u}_2}{l_s} \tag{21}$$

Substituting Equations 16 and 19 into Equation 21 gives the equation for the strain rate of the sample, Equation 21.

$$\dot{\varepsilon}_s = \frac{c}{l_s}(-\varepsilon_i + \varepsilon_r + \varepsilon_t) \tag{22}$$

By definition the forces in the two bars are given in Equations 23 and 24.

$$F_1 = AE(\varepsilon_i + \varepsilon_r) \tag{23}$$

$$F_2 = AE(\varepsilon_t) \tag{24}$$

Assuming that the two forces reach equilibrium after a finite amount of time, Equations 23 and 24 can be combined into Equation 25.

$$\varepsilon_t = \varepsilon_i + \varepsilon_r \qquad (25)$$

Substituting Equation 25 back into Equation 22, we get the final form of the equation

for strain rate of the sample, Equation 26.

$$\dot{\varepsilon}_s = \frac{2c\varepsilon_r}{l_s} \qquad (26)$$

By integrating Equation 26 with respect to time we can calculate the strain of the

sample at any instant in time as shown in Equation 27.

$$\varepsilon_s = \frac{2c}{l_s} \int_0^t \varepsilon_r \, dt \qquad (27)$$

The stress at the rear interface of the sample, denoted by the subscript s2, and the

transmission bar is shown in Equation 28.

$$A_s \sigma_{s2} = A_0 \sigma_t \qquad (28)$$

Assuming that the sample is in stress equilibrium, $\sigma_{s1}=\sigma_{s2}=\sigma_s$, Equation 28 can be

rearranged to form Equation 29.

$$\sigma_s = \frac{A_0}{A_s} \sigma_t \qquad (29)$$

Since σ=Eε, Equation 29 is reduced to its final form in Equation 30.

$$\sigma_s = \frac{A_0 E \varepsilon_t}{A_s} \qquad (30)$$

Therefore, the stress strain curve for the test specimen can be determined via

Equations 26, 27, and 30.

Chapter 2: Pulse Shaping

Introduction

In pseudo-static testing it is relatively easy to achieve a constant strain rate and stress equilibrium. The rate of change in length of the test specimen is tiny in comparison to the propagation velocity of stress waves and additionally the testing process is controlled with a feedback loop. Therefore, the strain rate can be very well controlled in these tests. In high strain rate testing the same assumptions cannot be made. The time needed for the propagation of stress waves is not negligible with Kolsky bar testing. The testing process is not controlled with a feedback loop and therefore the strain rate is not directly under control. Additionally, with high rates of strain, stress equilibrium within the sample is not instantaneous. To control the strain rate and to assist in rapidly reaching stress equilibrium we rely on pulse shaping.

Fundamentals

In a Kolsky bar test, the striker impacts the incident bar causing an elastic pressure wave to propagate down its length through the sample and into the transmission bar. These waves are measured by the attached strain gages. A typical set of signals from a test of a ductile material conducted without pulse shaping is shown in Figure 3. Note how the incident wave, ε_I, is approximately a square pulse. The pulse has a very short rise time, reaches its maximum value quickly, and has some high frequency oscillations. Since the leading edge of the pulse is very steep it represents an

instantaneously applied constant stress. This should be somewhat intuitive since neither the striker or incident bar are plastically deforming.

The response of the materials being tested, however, may not undergo strain in this manner. Many metals for example show what is known as a bi-linear response like the transmitted wave, ε_T, in Figure 3. The sample in this test underwent a rapid linear strain during its elastic response and then deformed plastically in a linear manner at a slower rate. Materials that are brittle, soft (plastic), or ductile all have different responses to stress, e.g. shapes of transmitted waves, and each have their own experimental techniques [3]. Brittle materials, for example have triangular shaped transmitted waves compared to the bi-linear or trapezoidal shaped waves of ductile materials [3]. This paper will only deal with techniques for testing ductile materials with strain hardening behavior.
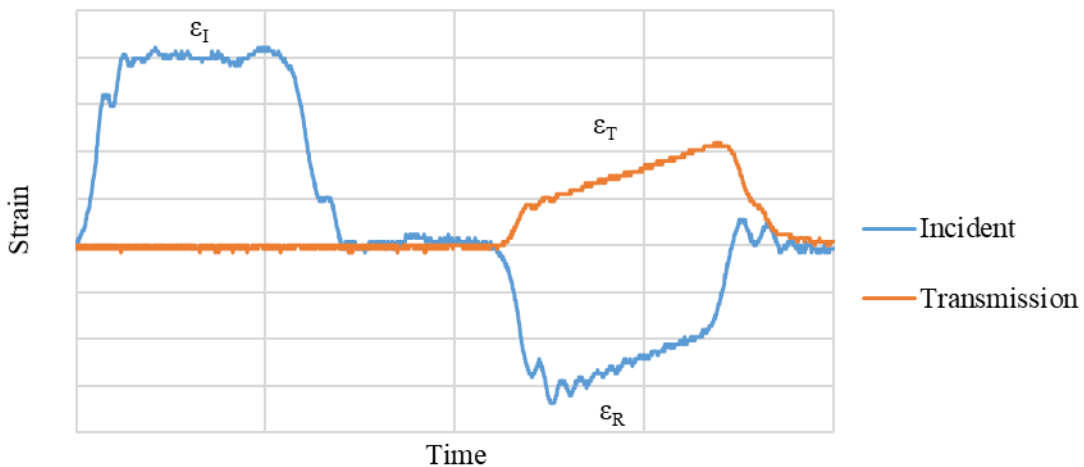
Figure 3. Kolsky Bar Test Conducted without Pulse Shaping

It was stated earlier that a constant strain rate is desirable to accurately describe the test conditions which produced a stress strain curve. To see how it is possible to achieve constant strain rate we need to look back at Equation 26. To achieve a

constant strain rate in the specimen, the reflected strain, ε_R, must be constant with respect to time. Rearranging and differentiating Equation 25 with respect to time gives Equation 31.

$$|\dot{\varepsilon}_r| = |\dot{\varepsilon}_i - \dot{\varepsilon}_t| \tag{31}$$

It is shown that for the strain rate to be zero, the slope of the incident and transmitted must be the same with respect to time. To put it into practical terms, if the profile of the incident wave and transmitted wave are similar in shape, then the reflected pulse, ε_R, will be constant with respect to time as seen in Figures 4, 5, and 6. Note that the magnitudes incident and transmitted waves will always be different due to the presence of the reflected wave. Therefore, the ultimate goal of pulse shaping is to alter the profile of the incident wave to match the shape of the transmitted wave, see Figure 6, so that the reflected wave is constant with respect to time which gives the test a constant strain rate.
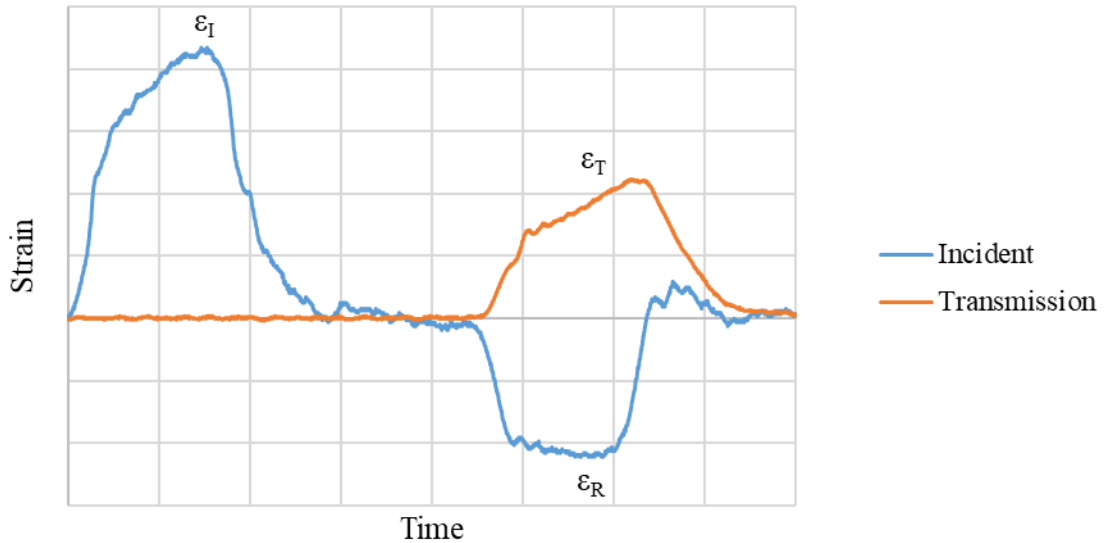
Figure 4. Kolsky Bar Test Conducted with Pulse Shaping
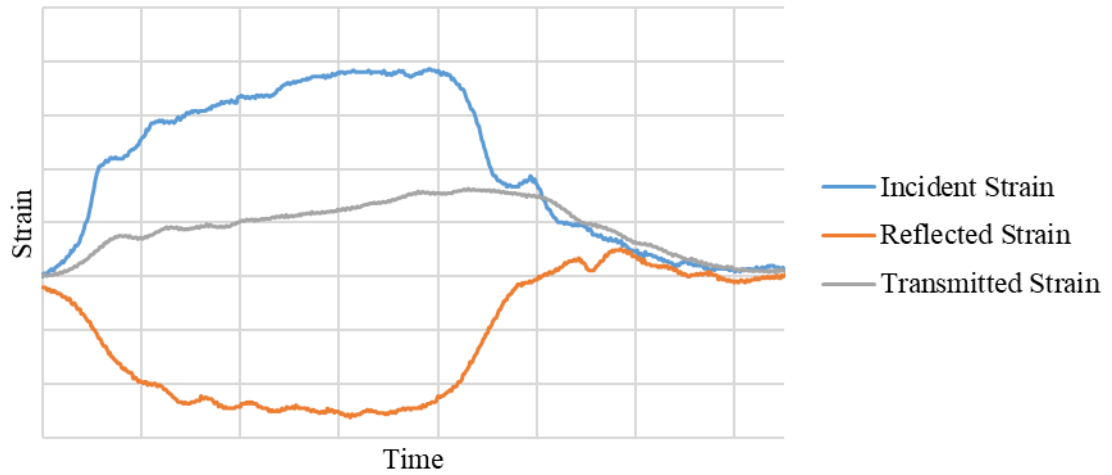
Figure 5. Test Signals Superimposed
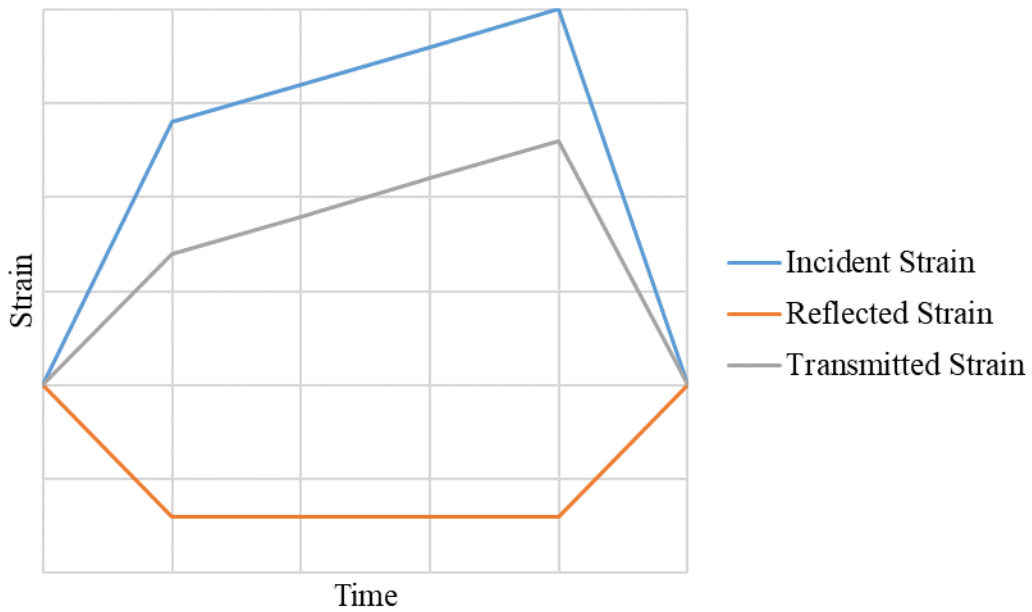
Figure 6. Idealized Test Signals Superimposed

Achieving a constant rate has been a historical issue. In previous decades the best

researchers could do was to take the time average of the strain rate [6,7]. However,

this is a questionable practice at best. A stress strain curve may be generated from the

test; however, it is difficult to accurately state the conditions under which it was

created when the strain rate has wild fluctuations. In the early 1970s researchers

invented a new technique to improve the strain rate called the three-bar technique,

shown in Figure 7. In theory, the best possible incident pulse shape would identically

mimic material response of the test specimen, shown by the transmitted pulse. It was

decided that one way to do this is was to use the transmitted pulse passing through a

dummy sample, made of identical material to the test specimen, as the incident pulse

for the test specimen.
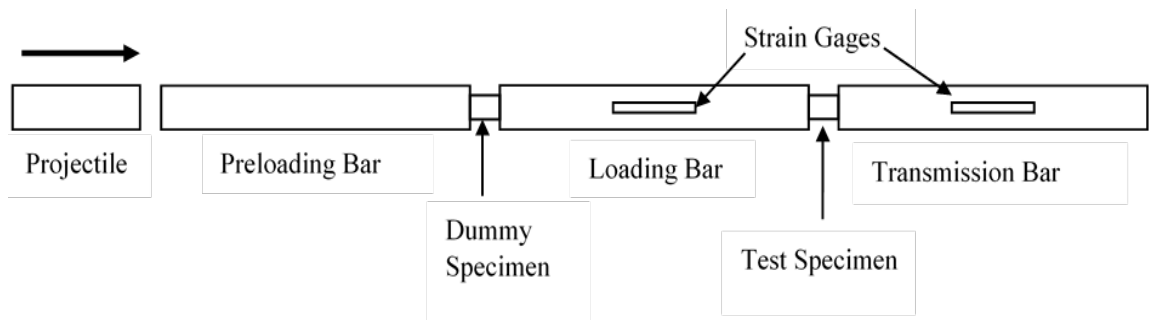
Figure 7. Three-Bar Test Technique Setup

The principle of operation can be illustrated by combining the material responses

shown in Figures 3 and 4 into a single test while using the terminology from Figure 7.

In a three bar test the projectile hits the preloading bar and creates an incident wave,

ε_I Figure 3. The incident wave travels through the dummy specimen as a transmitted

wave with a bilinear shape, ε_T Figure 3. This transmitted wave moves through the

loading bar and will be the incident wave for the true test specimen, ε_I Figure 4. This

shaped incident wave travels through the test specimen and into the transmission bar.

The transmitted wave, ε_T Figure 4, has a similar shape to the incident wave and thus

the reflected pulse is nearly constant with respect to time, ε_R Figure 4. This was a

huge improvement over the standard method of taking the average strain rate. Figure

8 shows how pulse shaping affects strain rate. Single and dual pulse shaping will be

discussed in a later section. The important thing to take away from this is that pulse

shaping increases the consistency of the strain rate with respect to time which is

highly desirable.
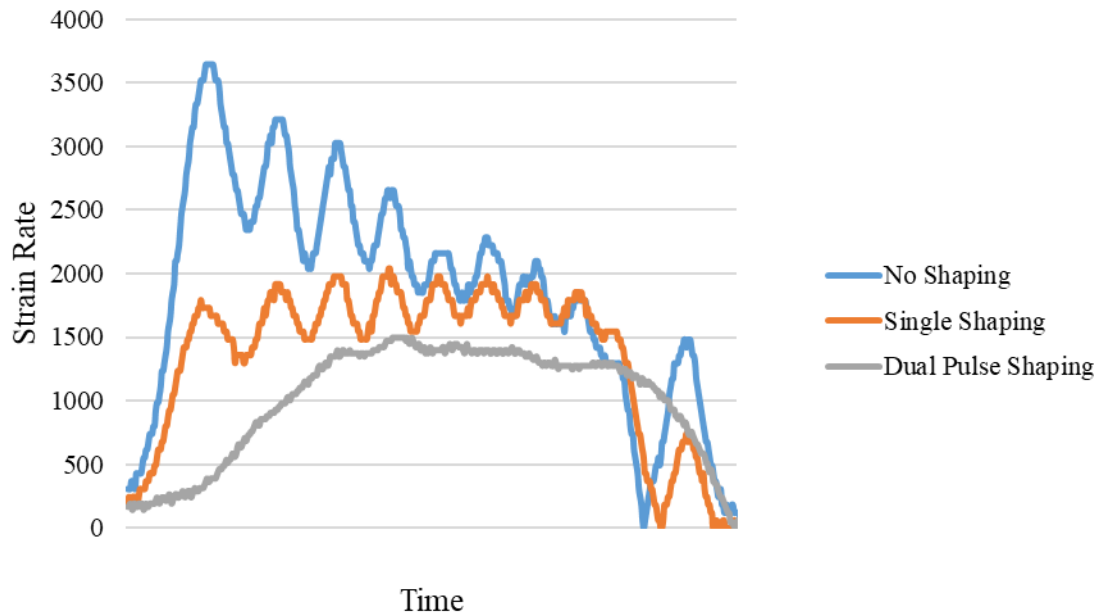
Figure 8. Strain Rate Profiles from Tests Conducted with and without Pulse

Shaping

Eventually it was determined that the preloading bar itself was unnecessary since the

projectile could impact the dummy sample itself and therefore the preloading bar was

eliminated from the setup. One disadvantage of using a dummy sample was that

twice as many test samples were needed to conduct testing. Additionally, it was

necessary to modify the geometry of the dummy specimen to fine tune the desired

shape and magnitude of the incident pulse for the test specimen, a tedious and

potentially very expensive process. This is not practical when the test samples are

costly or hard to manufacture.

It was later found that it was not necessary to use identical materials for the pulse

shaper (dummy specimen) and the test specimen. The important thing was that the

transmitted pulse from a pulse shaper was the appropriate shape and magnitude for

the test specimen's material response.

Depending on the test specimen material it may not be possible to produce an

appropriate incident pulse with a single pulse shaper. To further modify an incident

pulse may require the use of secondary pulse shaper made of a different material.

One such dual pulse shaper is a combination of steel and copper [8,9]. In this case,

the basic shape of the incident pulse is determined by the steel shaper and the copper

modifies the elastic response and pulse magnitude. Additionally, the softer copper

improves the damping out of high frequency oscillations in the incident pulse.

There are many considerations when designing a pulse shaper. First, and most

obviously, is the desired shape and magnitude of the incident pulse. This drives the

other considerations of pulse shaper material(s) and the shape/size of the pulse

shaper(s). Common materials include paper, aluminum, copper, steel, and plastics

such as nylon and Teflon [3]. Usually, the geometry of the pulse shapers are thin

disks. The combinations of size and material for single and dual pulse shapers are

almost limitless and there may be several combinations which produce similar results.

With respect to size, it has been shown experimentally that pulse shaper disks cannot

be scaled up indefinitely as shown in Figure 9. A small diameter pulse shaper may

give a smooth pulse while a larger diameter of the same thickness may have the same

general shape but is very jagged. This phenomena has been investigated and is a

product of radial inertial forces [10–12]. When the diameter of the shaper is small the

radial forces are negligible but when the diameter increases, they become significant. This effect was noted during testing but was not significant. One method to alleviate this is to use multiple small pulse shapers in place of one large pulse shaper as shown in Figure 10. However, this has limited practicality unless the dimeter of the incident bar is very large. The bar diameter shown in Figure 10, for example, is three inches. Another method to reduce the effects of radial inertia is to use an annular shaped pulse shaper. With these it is possible to increase the surface area and volume of the pulse shaper while keeping the inertial forces low. A comparison of the distribution of radial inertial forces between solid and annular pulse shapers is shown in Figure 11. The representative incident pulses created by these pulse shapers is shown in Figure 12. Again, this technique is better suited to large diameter bars and was not used in this series of tests.
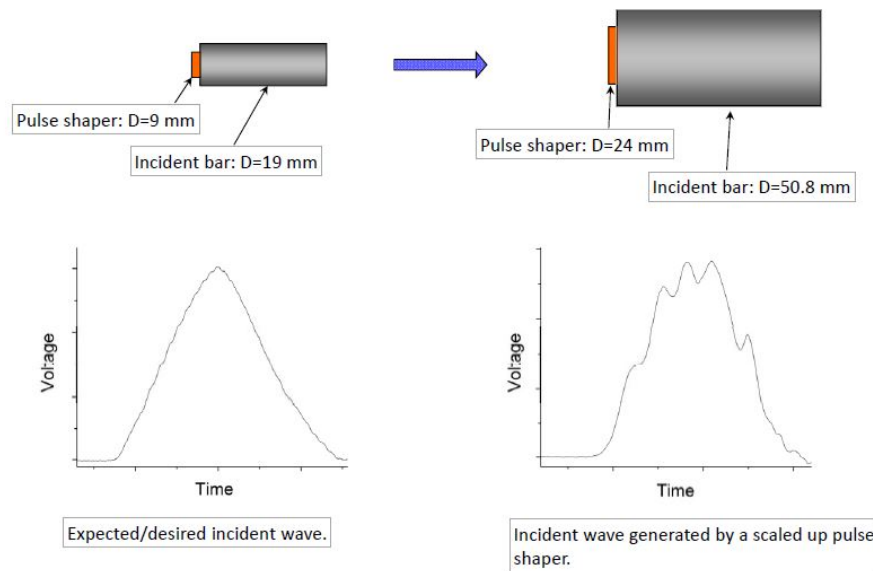

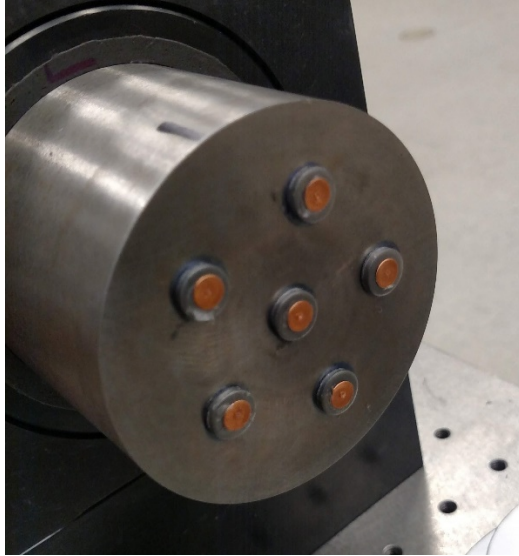**Figure 9. Non-linear Effects of Scaling Up Solid Pulse Shapers** [11]

Figure 10. Use of Multiple Small Pulse Shapers in Place of one Large Pulse Shaper
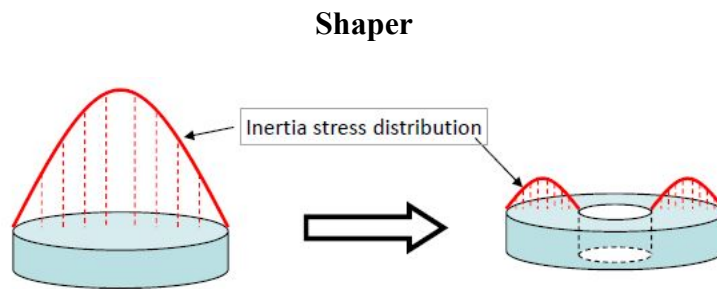

Figure 11. Distribution of Radial Inertial Stresses for Solid and Annular Pulse Shapers [11]
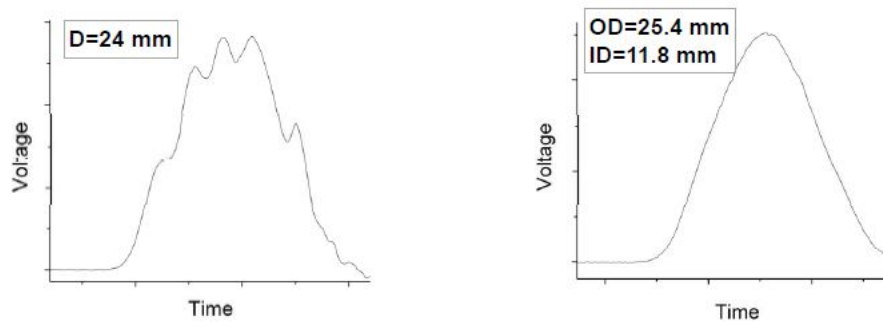

Figure 12. Incident Pulses Generated by Solid and Annular Pulse Shapers [11]

Pulse Shaping Design

As numerous previous studies have shown the design of a pulse shaper, meaning the materials and dimensions, depends on the stress-strain response of the material to be tested as well as the desired strain rate of the experiment [13]. Again, the most common way to design and fine tune a pulse shaper is through trial and error. Several attempts at creating an analytical model of a pulse shaper have been performed with the hope of creating a computer program that will design pulse shapers *a priori* [8,9]. These have been successful in approximating the behavior of a pulse shaper and giving an approximate design. However, these programs have significant drawbacks. The material property of the test specimen as well as the pulse shapers must be known ahead of time. Additionally, the heat treatment or cold working of any of these materials may significantly alter its properties. Therefore, the computer programs may be able to provide good starting points under certain conditions; regardless, the final design still needs to be found through trial and error. Naghadabadi et al. (2012) discussed general guidelines for designing a single pulse shaper. First, it is important to understand make-up of the incident pulse itself before describing how pulse shaping affects it. A typical shaped incident pulse has four components as seen in Figure 13. The first component, denoted A, is the elastic deformation of the pulse shaper which is usually linear. The second, B, is the plastic deformation of the pulse shaper. This too may be linear and is less steep than the elastic region. The third, C, is the rigid mode of the pulse shaper. This occurs when the pulse shaper reaches its maximum plastic deformation and behaves as an incompressible solid. Depending on the duration of the incident pulse, this region

19

may not exist if the pulse is too short. Lastly, there is the elastic rebound of the pulse shaper, D, which is generally not considered important.
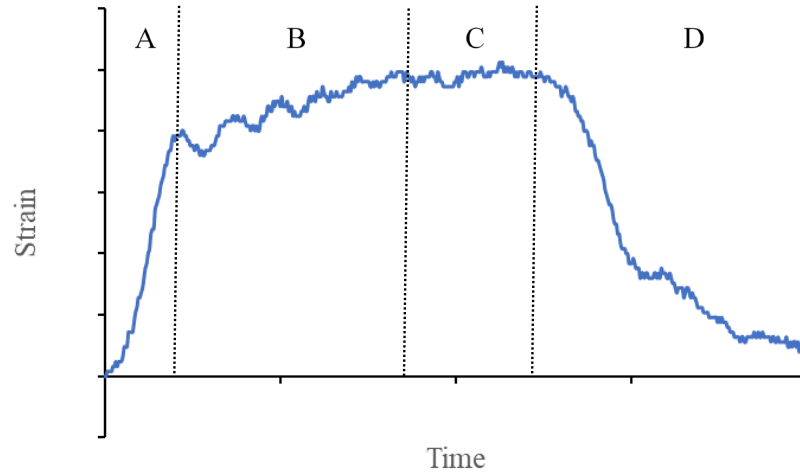

Figure 13. The Four Material Responses Shown in a Shaped Incident Pulse

There are many components to single pulse shaper design but the four that will be discussed are pulse shaper thickness, pulse shaper diameter, striker length and striker velocity. As discussed by Naghadabadi et al., the thickness of the pulse shaper increases the rise time, which is the time it takes to reach the end of region B, as well as increasing the overall pulse duration. Conversely, increasing the diameter decreases the rise time and pulse duration. Additionally, changing the diameter alters the magnitude of the transition from elastic to plastic behavior, the end of region A. Increasing the striker velocity decreases rise time. Lastly, increasing striker length increases pulse duration. The effects of changing pulse shaper diameter and thickness will be demonstrated in the next section.

As a general rule, the dimensions of the pulse shaper are dictated by the work hardening behavior of the test material. For low work-hardening materials a large diameter and small thickness are recommended. For moderate work-hardening materials a large diameter and large thickness are recommended. Lastly, for high work-hardening materials a large thickness and small diameter are recommended [13].

After a suitable pulse shaper has been found, Naghdabadi et al. also gave some simple guidelines for scaling the pulse shaper for new test conditions. The pulse shaper thickness and cross-sectional area can be scaled to the striker velocity while the thickness can be scaled to the striker length. As always, these guidelines only give a starting point for the next pulse shaper design to be fine-tuned by trial and error.

Single Pulse Shaping Experiments

The effects of single pulse shaping are shown in Figures 14 and 15. It is easily noted that drastic changes in pulse shape are possible by modifying the dimensions of the pulse shaper. The behavior of the pulse shaped signals duplicates the findings of Naghdabadi et al. The changeover point from elastic to plastic is modified by changing pulse shaper thickness as seen in Figure 14. The smallest diameter shaper is shown by the nearly triangular pulse. As the diameter increases the radial inertial forces also increase in effect making the pulse shaper "harder". The rise time and magnitude of a pulse is altered by changing diameter as seen in Figure 15. As the thickness increases the pulse shaper is able to deform more before becoming ridged and therefore it absorbs more energy which lowers the magnitude of the incident pulse. It is important to note that while the high frequency oscillations are usually

greatly reduced from unshaped to shaped pulses, they are generally not completely eliminated. This may cause unwanted oscillations in the strain rate of the test. Dual pulse shaping can help further reduce oscillations and modify the pulse shape. This will be talked about in the next section.
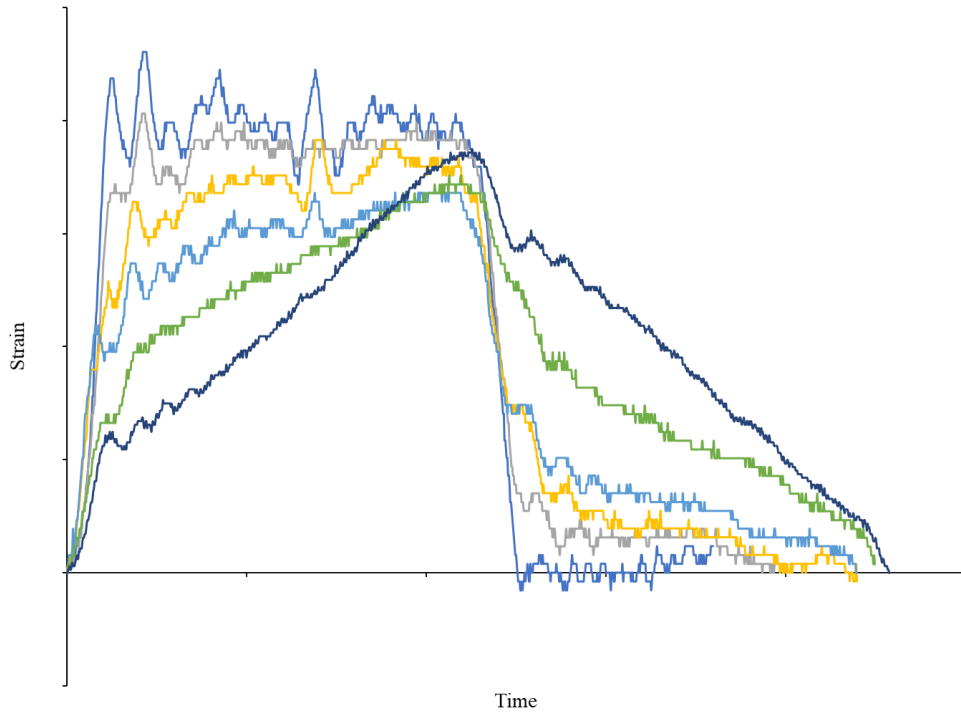

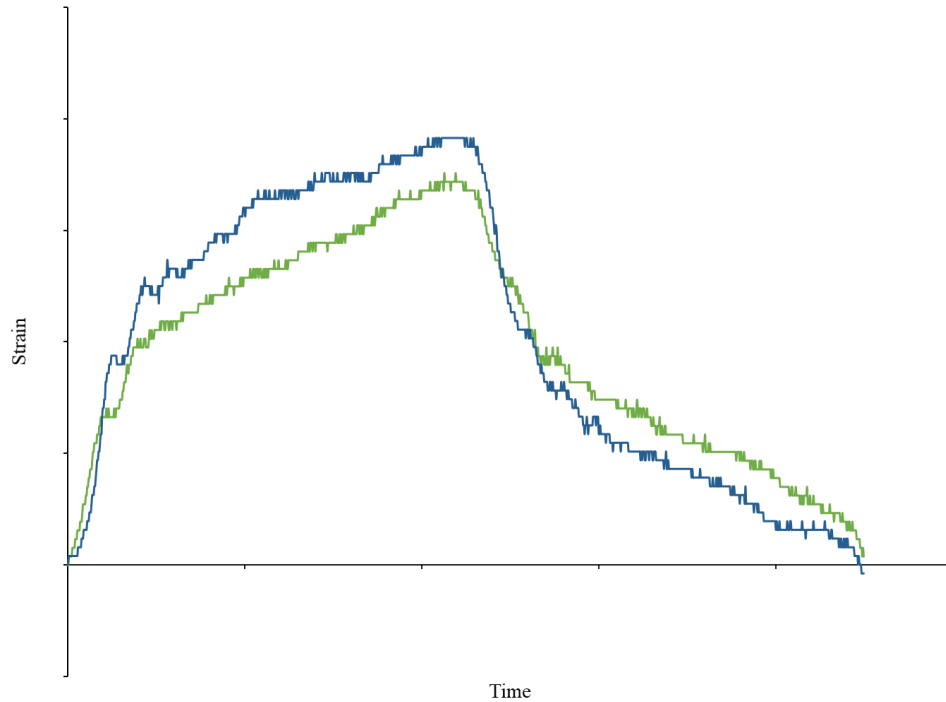**Figure 14. The Effect of Changing Pulse Shaper Diameter on the Incident Pulse**

Figure 15. The Effect of Changing Pulse Shaper Thickness on the Incident Pulse

Dual Pulse Shaping Experiments

Additional modification of the pulse can be achieved when using dual pulse shaping as opposed to single pulse shaping. Some of these effects can be seen in Figure 16. In this test, a steel pulse shaper is paired with an aluminum pulse shaper. The addition of the aluminum pulse shaper further modifies the elastic to plastic transition point, the rise time, and the magnitude. With the right combination of dual pulse shaper geometries, the elastic to plastic transition point can disappear and the strain becomes linear with respect to time. This linear strain behavior is useful for brittle materials such as concrete.
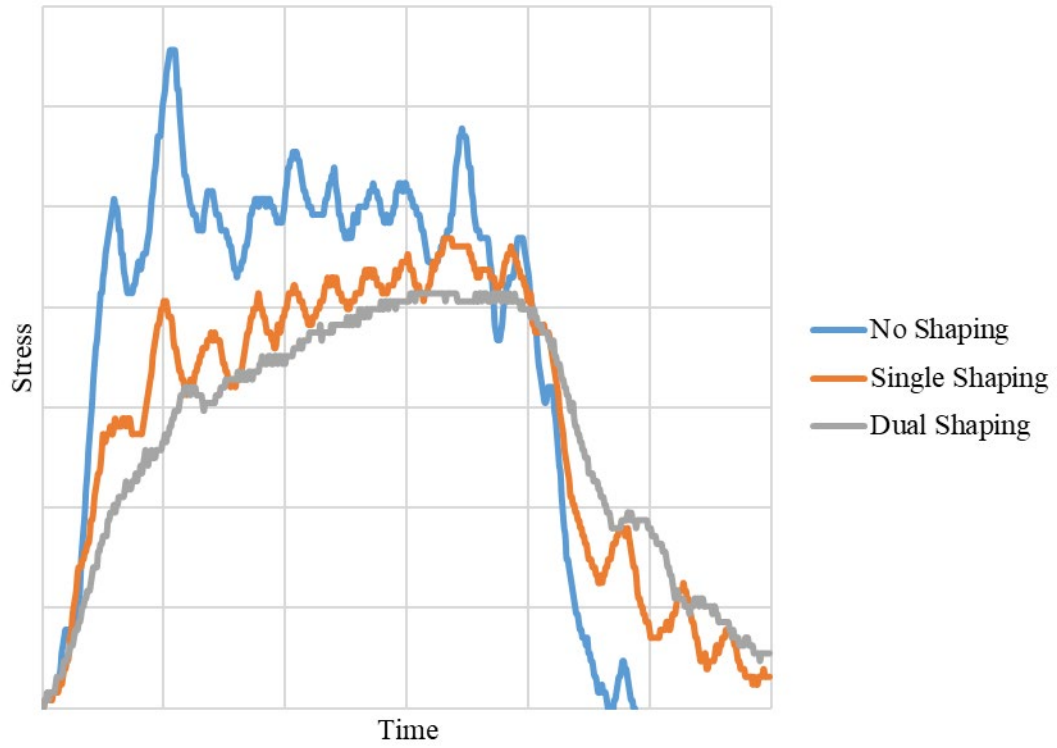
Figure 16. The Effects of Dual Pulse Shaping on the Incident Pulse

Chapter 3: Introduction to Additive Manufacturing

Introduction

Many of the traditional methods of manufacturing have been around for thousands of years. Subtractive manufacturing methods, include milling, turning, and drilling, remove excess material from a larger piece of raw material to form a finished part. These methods can be slow, can produce a lot of waste, and are limited in the geometry of the parts they can produce by tooling and techniques. Joining methods include welding, brazing, riveting, and fastening. These methods mate several simple parts into a single part or combine individual parts into an assembly. However, the more joints and connections a part or assembly has, the number of possible failure points increase. Formative methods include forging and casting. These methods can create strong components but again the possible geometries are limited and not all materials are well suited to forming methods. Additive manufacturing (AM), on the other hand, has the ability to create intricate and complicated part geometries that are impossible with traditional manufacturing methods with fewer weak points (joints) and with little to no waste. AM has the potential to create stronger, lighter, and more complex parts than could ever be made by traditional means, properties that are of great interest to the aerospace community.

Additive manufacturing is a process in which an object is created, or printed, by adding thin layers of material on top of each other to create a solid object. AM is known by several additional names including 3D printing, rapid prototyping, and direct digital fabrication to name a few. It was first developed in the 1980s to rapidly

create crude prototypes but now the technology has improved to the point where fully functional metal components can be produced [14]. The surface quality and material properties of the printed part are a product of several factors: the printing process utilized, the printing parameters, the building material, the print layer thickness, the ability of the layers to adhere to each other, the microstructure of the printed material, the residual stresses in the final product, build orientation, and the porosity within the final product. Many optimization studies have been conducted to determine the best combination of process, material, print parameters, and post processing to produce components with the highest density and best material properties. But there is inevitably variation from machine to machine, batch to batch, and material to material.

Two Additive Manufacturing Processes

There are several different kinds of AM processes in use today, however, only two will be discussed. The first one that usually comes to mind is material extrusion, where layer upon layer of molten plastic is used to build a component from the bottom up. This is the one most likely to be owned by hobbyists due to its relative simplicity and low cost. However, its ability to produce high-quality and functional components is limited due to its limited material choices and low print resolution. When it comes to printing metals the options are pretty limited. When balancing print quality, material choice, resolution, post processing requirements, and cost, laser powder bed fusion processes (LPBF) are the most popular. This process has been used to manufacture components in stainless steel, tool steels, aluminum, titanium alloys, cobalt chrome, and nickel alloys to name a few [15]. Like material extrusion,

the component is built in thin layers from the bottom up. However, this is where the similarities stop. A typical LPBF printer is shown in Figure 17. The print process begins when the build plate on which the part is printed is covered with a thin layer of metal powder by the powder roller. A high-power laser beam is reflected off of a movable mirror on to the surface of the powder. This beam is used to melt the powder into a small melt pool in the path of the laser. As the laser moves the melt pool cools and a solid is formed in the areas where the powder was melted. Once a layer of powder has been melted, the build plate moves down and is covered with another fine layer of powder by the roller which will in turn be melted. This process is repeated from hundreds to thousands of times until the part has been produced.
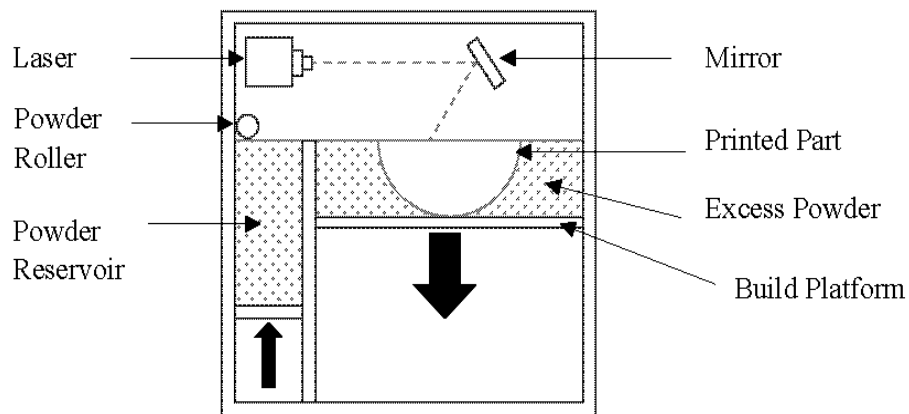
Figure 17. Schematic of a Laser Powder Bed Fusion Printer

Ideally, the parts produced via LPBF would be fully dense, have the same material properties as a regularly manufactured part, would have a surface finish that requires no post processing, and would not require heat treatment. However, this is not the case, at least not yet. Many parts produced will need varying levels of post processing treatments before they are ready for use.

Laser Powder Bed Fusion Print Parameters

One of the main goals when printing metals is to create parts that are fully dense. This occurs when all of the powder in the part is fully melted, the print layers are well bonded, and there are no voids within the component itself. The way these factors are controlled are through adjusting the print parameters. Parameters that affect density include laser power, scan speed, laser width or diameter, layer height, and hatch length, which is also called hatch spacing or pitch. These parameters must be carefully balanced to produce high quality parts. Note- there it no universal terminology for the print parameters within the AM community. The same parameter may have several different names depending on which specific process it is referring to. This leads to some inconsistency and confusion with terminology.

Work by Mutua et al. and others show that there is an optimum combination of print parameters to produce nearly fully dense parts [16]. It is important to note, however, that this optimum value will vary from machine to machine and will be different for every print material. Additionally, these parameters are not independent of each other. A change in on parameter may require the adjustment of one or more other parameters to achieve good results.

Despite its impracticality we can see what effect changing one parameter at a time can do to the porosity of the final product. When looking at the power of the laser, it must be sufficient to melt all of the powder in its path or else there will be un-melted powder and/or poor fusion between layers. Conversely, if the laser power is too high the temperature in the melt pool will become exceedingly hot and produce strong convection currents, vaporization, and splattering of the molten material, all of which

lead to porosity [17]. The scanning speed has similar temperature effects. If the speed is too slow then the temperature in the melt pool will be too high, and if it is too fast the temperature will be too low. The layer height must be sized such that all of the powder in the layer is melted as well as a portion of the layer below it. This condition leads to excellent bonding between layers. However, if the layer is too thick, adequate powder melting and bonding between layers does not occur. When the powder layer is too thin the temperature in the melt pool again becomes too high. The laser diameter and hatch spacing have opposite effects as shown in Figure 18. If the laser diameter is too large or the hatch spacing is too small there will be excessive overlap between rows leading to excessive temperature in the melt pool. When the laser diameter is too small or the hatch spacing is too large there may be inadequate melting between the rows.
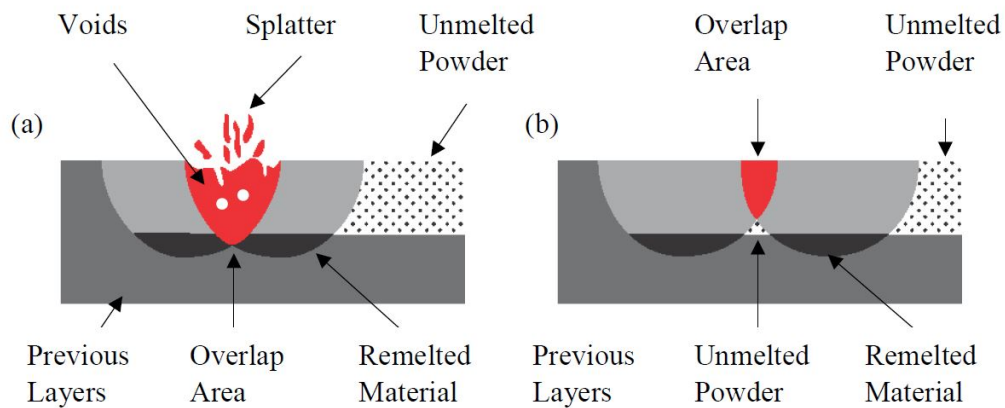
Figure 18. The Effects of Changing Hatch Spacing: (a) too close, (b) too far apart

Many research papers combine laser power, laser diameter, scanning speed, and hatch spacing into a single parameter called energy density. This quantity is the energy absorbed by the powder and is typically measured in J/mm^3. This simplification can,

while generally useful, lead to problems. It is possible to have the same energy density from drastically different print parameters. Research by Mutua et al. shows that it is possible to have very different part densities from similar energy densities which is problematic [16].

3D Systems ProX 200

The printer used during this study was the 3D Systems ProX 200 shown in Figure 19. It utilizes a 300-Watt fiber laser with a wavelength of 1070 nm. It has a print volume of approximately 140x140x100mm. The typical total dimensional accuracy of this machine is within 50μm.

Figure 19. 3D Systems ProX 200

Chapter 4: About Inconel 625

Material Description and Uses

Inconel 625 (IN625) is a nickel-based superalloy which is able to operate over a wide temperature range, from cryogenic temperatures to 1000+ °C [18]. It has good tensile, yield and creep strengths as well as high corrosion resistance, even while at high temperatures in harsh chemical environments [19]. These properties make IN625 an excellent material for use in extreme environments common in many industries such as nuclear, marine, chemical and aerospace for parts such as heat exchangers, valves, piping, blades, fittings, and seals [20–22]. Due to its work hardening behavior, high hardness, high-temperature strength, and low thermal diffusivity, IN625 is difficult to machine via subtractive methods which leads to high tool wear and low material removal rates [15,18,22]. Additionally, the quality of forgings and castings is difficult to control [19]. The demand for increasingly complex part geometries and IN625's easy weldability therefore makes it a good candidate for LPBF techniques[18].

Composition and Properties

IN625 is a solid solution of many elements as seen in Table 1 [23]. These elements, even in trace amounts, alter and improve the material properties. For example, chromium, molybdenum, and iron are all solid-solution strengtheners. Aluminum, titanium, and niobium all form nickel compound precipitates which increase strength.

31

Aluminum and chromium improve oxidation resistance. While some elements improve the material properties, others, such as oxygen and sulfur, are deleterious and should be tightly controlled [23]. Selected material properties for IN625 are shown in Table 2.

Ni	Cr	Mo	Nb	Al	Ti	Fe	Mn	Si	C
61.0	21.5	9.0	3.6	0.2	0.2	2.5	0.2	0.2	.005

Table 1. Composition of Inconel 625 [23]

Material Property	SI Units	English Units	Test Temperature
Ultimate Strength	965 MPa	140 ksi	@ 21°C (70°F)
Yield Strength (0.2%)	490 MPa	71 ksi	@ 21°C (70°F)
Dynamic Modulus	208 GPa	30.1×10^6 psi	@ 21°C (70°F)

Table 2. Selected Properties of Wrought Inconel 625 [23]

Microstructure

The macroscopic properties of a material are significantly influenced by its microstructure [19]. For the purposes of this study, it is important to understand that the microstructure of AM components is different than forged materials and this largely explains the differences in material properties.

IN625 is a nickel solid-solution alloyed with chromium, molybdenum, and other elements dissolved into the matrix. These elements also combine to create precipitates, the type and location of which alter the material properties of the material as a whole. The heat treatment and manufacturing method largely determine which precipitates are present and the crystalline structure of the matrix.

When examining the microstructure of an AM material, one of the most readily evident properties is porosity. Forged materials, due to their manufacturing process, are fully dense. Therefore, AM materials that are not fully dense are not maximizing the limits of their potential material properties. Considerable research has been directed at reducing the porosity of AM materials in general, including IN625. These studies vary the print parameters, such as laser power, scan speed, hatch length, etc., to experimentally determine the best combination of parameters to minimize porosity since analytical models of the melt pool don't yet exist. Unfortunately, these combination of print properties are not always transferrable from machine to machine. However, it is now possible to produce nearly fully dense parts with relative densities >99.8% [18,22].

Several phases can exist within the IN625 molecular structure [23]. The matrix of IN625 is a face centered cubic (fcc) nickel-base phase called gamma, γ. This is the matrix into which the solute elements are diffused. The second phase is gamma prime, γ'. This is an fcc precipitate of nickel and either aluminum, titanium, niobium, and chromium which adds high temperature strength and creep resistance. Another precipitate is gamma double prime, γ". This is a metastable, base centered tetragonal (bct) Ni_3Nb precipitate which adds strength at low temperatures. After prolonged exposure to sufficient heat γ" will transform to the equilibrium δ phase which is orthorhombic. While the δ phase can improve the tensile strength, it comes at the cost of reducing the elongation and toughness [24]. Lastly, carbides form with reactive elements such as titanium and niobium [23].

Research by Li et al. finds that, due to the rapid cooling of IN625 during the printing process, most of the solute atoms, i.e. chromium, molybdenum, and niobium, remain trapped in the nickel matrix and do not have sufficient time to form other phases or carbides [19]. Unlike in its wrought counterpart, the solute molecules in AM IN625 are not homogeneously spaced but rather show micro-segregation. This micro-segregation can be partially homogenized with heat treatment.

Due to the residual stresses within the test specimen from the printing process as well as to improve the ductility and fatigue life of an AM component, it is necessary to heat treat printed parts before they begin their service life. Additionally, heat treatment can cause the crystalline structure to recrystallize, improve grain size, reorient grains, change the types and quantities of precipitates [19,21]. These improvements also have the effect of reducing, but not eliminating, the anisotropy of AM materials.

Previous research has shown that significant changes in microstructure take place during heat-treating processes. Micrographs of the samples used in this study were not taken, however, Figures 20 and 21, taken from Li et al (2017), show the significant microstructural changes that occur during a similar annealing procedure [21]. Figure 20 shows the microstructure of as printed Inconel 625. Figure 20(a) is taken parallel to the build layers with the build direction oriented upwards in relation to the picture. This shows the classic fish scale pattern from the addition of build layers. Figure 20(b) is taken perpendicular to the build layers, the build direction is towards the camera, and this shows multiple paths, or tracks, of the laser.
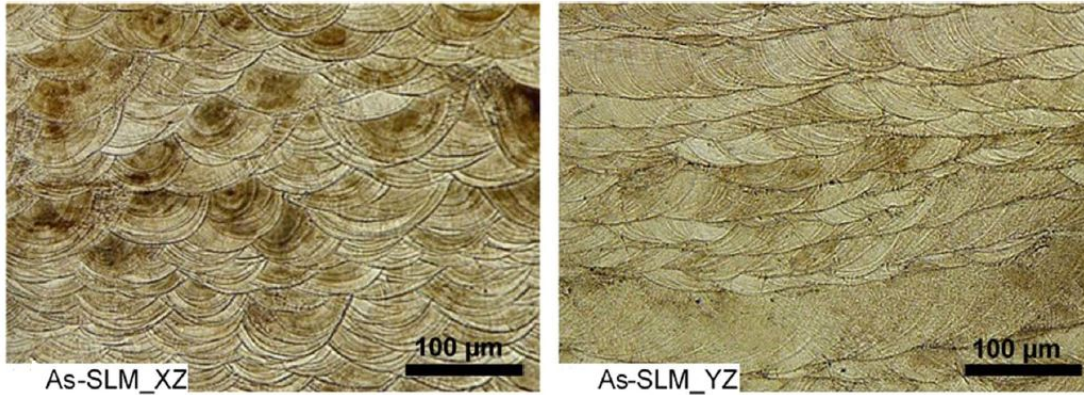
Figure 20. Microstructure of As Printed Inconel 625: (a) parallel to the build layers, (b) perpendicular to build layers [21]

Figure 21 shows AM Inconel 625 after annealing for 1 hour at 980° C. Note that this is a slightly different annealing temperature than was used for the samples in this study. The fish scale pattern and laser tracks are significantly faded after annealing. After further heat treatments they would be obscured completely.
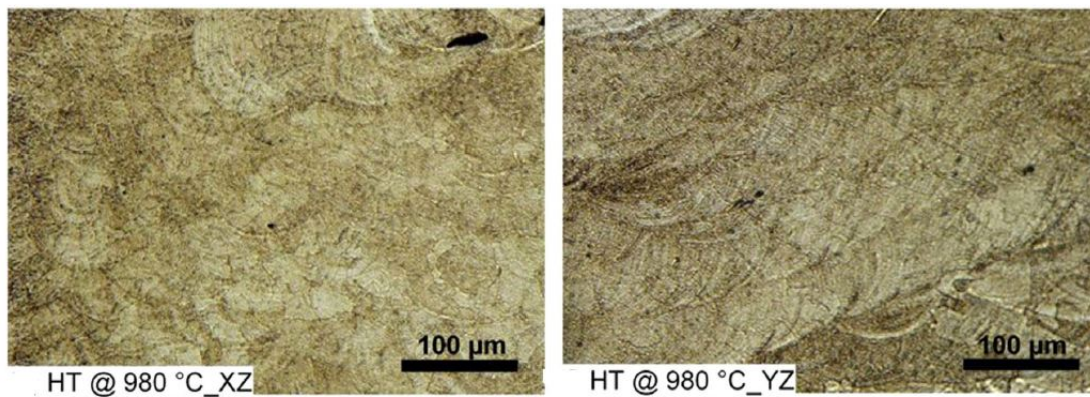
Figure 21. Microstructure of Annealed AM Inconel 625: (a) parallel to the build layers, (b) perpendicular to build layers [21]

Now that is understood that the heat treatment of a material strongly influences its microstructure and microstructure strongly influences its material properties it is time to look at the differences between AM and wrought IN625.

It has been shown repeatedly that AM materials show anisotropic behaviors due to their layered construction and their unique microstructures due to their rapid cooling [15]. AM IN625 is no different in this respect. The elastic modulus, yield strength, and ultimate strength are all dependent upon the test direction with respect to the build orientation as well as the print parameters and subsequent heat treatment. This anisotropy typically remains even after heat treatment [20,25]. Additionally, as shown in Table 3, the yield and ultimate strengths of AM IN625 are typically higher than forged IN625, which has better elongation and fatigue [19,21,22]. Despite the strength of as printed AM IN625, it is desirable to heat treat it to reduce the internal stresses from printing and modify the microstructure to achieve the appropriate combination of strength, ductility, and fatigue life desired for a specific purpose [21,22].

Material Properties	Wrought (annealed) [23]	AM Horizontal (annealed) [20]	AM Vertical (annealed) [20]
Yield Strength (MPa)	455	640±20	600±20
Ultimate Strength (MPa)	965	1030±20	980±20
Elongation at break	50%	27±3%	34±3%

Table 3. Comparison of Selected Material Properties of Wrought and Additively Manufactured IN625

Chapter 5: Experimental Set up

Sample Creation

The AM produced tension samples, shown in Figure 22, were printed on the University of Maryland's ProX 200 by 3D systems. The powder used was LaserForm Ni625(A) which is designed specifically compatible with this printer. The print settings used to produce the samples are shown in Table 4. Due to the limited build volume of the 3D printer the total length of the specimen was limited to approximately 3.5 inches. Therefore, the gauge section length is 1 inch long with 0.25-inch width. The test specimens were annealed at 1000° C for 1 hour [22,26]. The annealing process changed the color from a dull light gray to almost black. After annealing the samples were cut to a thickness of 0.08 inches with an electrical discharge machining machine, generally referred to as an EDM machine or EDM cutter, which uses an electrical current rather than a physical tool bit to remove material.
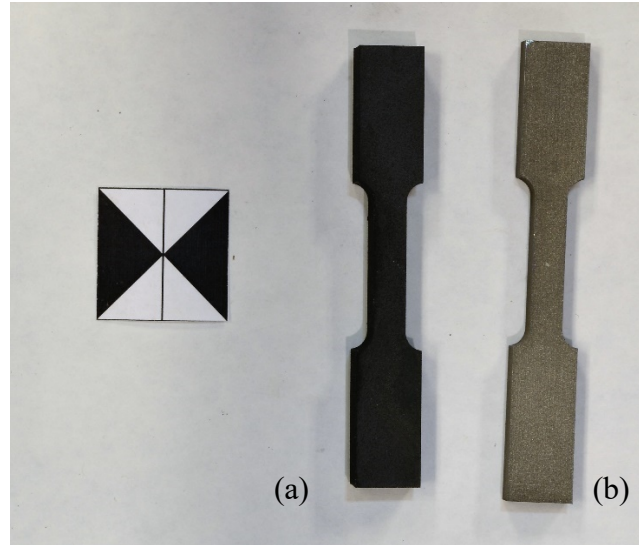
Figure 22. Additively Manufactured IN625 Tensile Test Samples: (a) horizontally printed and annealed, (b) vertically printed, not annealed, not used for testing

Print Parameter	Parameter Value
Laser Power	100%
Scan Speed	2500 mm/s
Hatch spacing	50 μm
Layer height	30 μm
Hatch Pattern	Hexagon

Table 4. Print Parameters Used for Test Sample Creation

ASTM B-446 compliant, half inch diameter IN625 rod from Rolled Alloys was used to create two tension samples as shown in Figure 23. A CNC lathe was used to machine the profile of the test specimens. The gage section had a 0.2-inch diameter and a 2-inch length. A 0.25-inch radius fillet was used to blend the gage section into the body of the test specimen. This specimen was annealed at 1000° C for 1 hour.
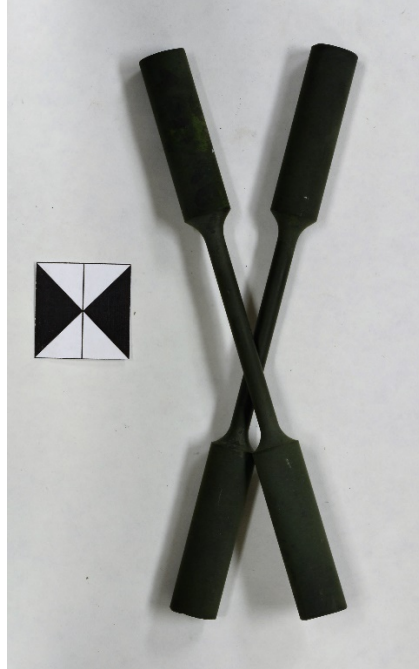
Figure 23. Wrought IN625 Tensile Test Samples: annealed

The AM produced compression samples were made from the same LaserForm Ni625(A) as before. The print settings used to produce the samples are also shown in Table 4. The specimens, shown in Figure 24, were 0.25 inches in diameter and 0.25 inches tall. Specimens were manufactured in both the horizontal and vertical orientations. The surface of the printed specimens is very rough and therefore were put in a lathe to smooth the ends of the specimen to produce a uniform contact surface. Lastly, the specimens were annealed at 1000° C for 1 hour to relieve internal stresses and make the specimens more comparable to annealed wrought material.
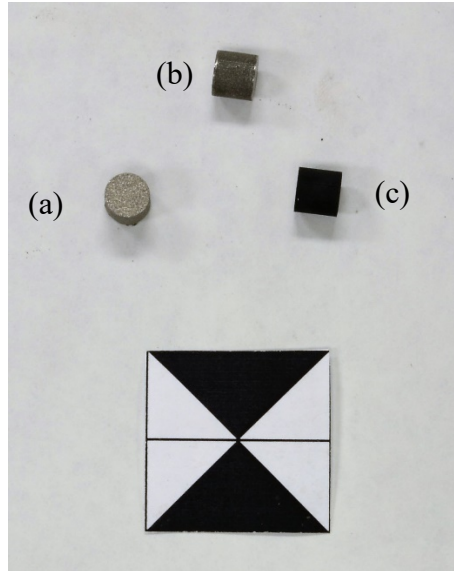
Figure 24. Additively Manufactured IN625 Compression Test Samples: (a) as printed, note rough surface finish, (b) machined ends, not annealed, (c) machined ends and annealed

Wrought 0.25-inch diameter rod IN625 rod purchased from Best Stainless and Alloy was used to create the compression samples shown in Figure 25. The ASTM B-446 compliant rod was cut into sections and then machined in a lathe to flatten and smooth the ends of the sample. The specimens were subjected to the same 1000° C annealing procedure as before.
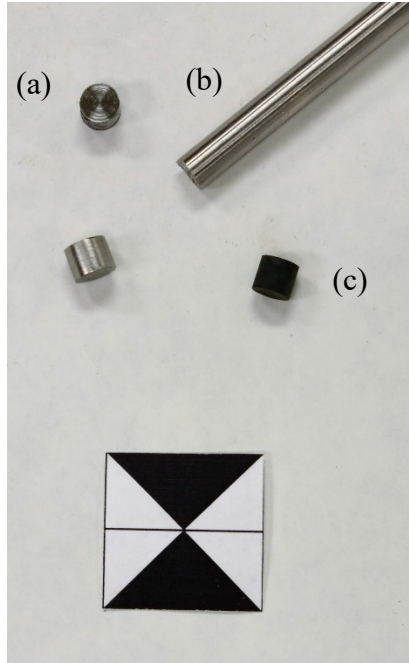
Figure 25. Wrought IN625 Compression Test Samples: (a) machined, not annealed, (b) round bar stock, (c) machined and annealed

Hardness Tests

Hardness testing was conducted using a United Tru-Blue Universal testing machine shown in Figure 26. Specimens were tested using the Rockwell A scale before and after annealing and the results are shown in Table 5. The hardness measurements for the AM specimens were consistent with values reported from both the literature and the manufacturer. Additionally there was no significant difference in hardness between print directions [19,20,22].
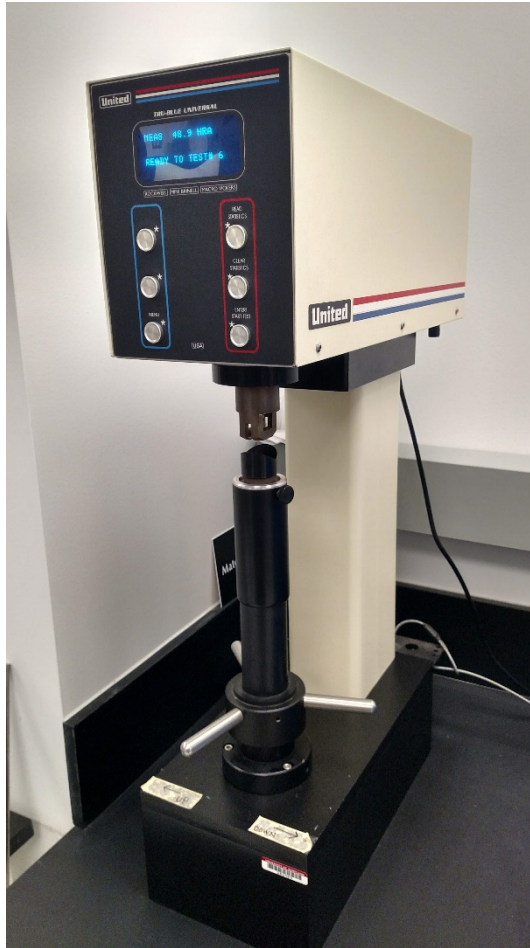
Figure 26. United Tru-Blue II Universal Hardness Tester

Sample Type	Average Hardness Before Annealing (Rockwell A)	Average Hardness After Annealing (Rockwell A)
Wrought Tensile Specimens	47.3	36.8
Wrought Compression Specimens	54.3	55.5
AM Specimens	61.0	63.0

Table 5. Average Hardness Measurements of Test Specimens

Tensile Tests

The tensile tests were conducted using a Tinius Olsen Universal Testing Machine shown in Figure 27. The machine was used in conjunction with clip on extensometers to measure specimen deformation. The testing rate was set at 0.1 inches of extension per minute up to 1.5% elongation and then 0.2 inches of extension per minute until failure.

Figure 27. Tinius Olsen H25K-T Benchtop Universal Testing Machine

Compression Tests

The Kolsky bar setup used for this study is shown in Figure 28. The gas gun is powered by a nitrogen tank and has a quick acting valve operated by a separate nitrogen tank. The barrel is nine feet long and fires Delran saboted projectiles at the incident bar. Pulse shapers were held to the end of the incident bar, and lubricated to reduce radial friction during deformation, with the aid of grease. Both the incident bar and transmission bar are 5/8" diameter and 48" long. The bars are supported by

linear bearings made of Delran. The strain gage pairs are mounted across from each other, centered 24" from the specimen contact surfaces. Again, the sample was held in place and lubricated with the aid of grease as shown in Figure 29. The strain gages are Micro-Measurements model CEA-13-062UW-350 which have a resistance of 350Ω each and a gage factor of 2.170. The adhesive is M Bond AE-10 from Vishay and the gages were installed following the installation instructions given in Vishay bulletin B-137. The connections from the strain gages were connected to a box containing internal 350Ω resistors to create a Wheatstone bridge. The bridge was connected to a Vishay 2310A Signal Conditioning Amplifier which powered the circuit and amplified the signal. The amplified signal was then sent to a LeCroy 9354AM oscilloscope operating at 5MHz for measurement and recording. The signal data was then exported to a custom Excel spreadsheet for processing.

Figure 28. Kolsky Bar Used to Conduct Testing
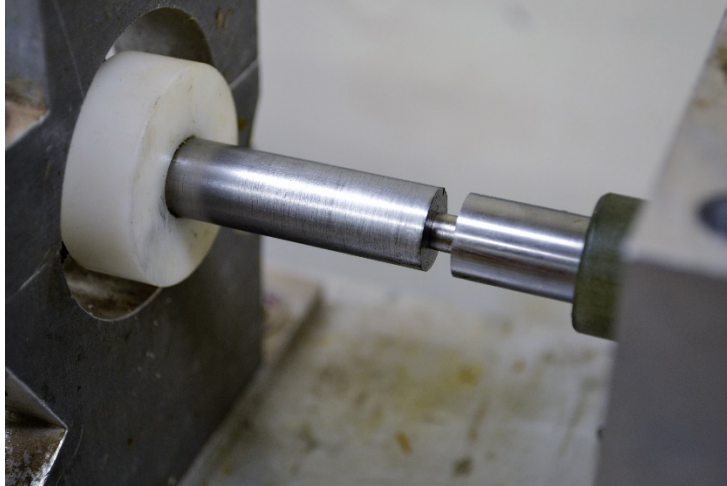
Figure 29. Compressive Test Specimen Installed and Ready for Testing

Pulse Shaper Fabrication and Design Process

Pulse shapers, shown in Figure 30, were fabricated from sheet steel ranging in thickness from 0.01 to 0.06 inches and from aluminum in ranging 0.006 to 0.01 inches. Diameters tested ranged from 5/32" to 1/2". They were punched out with a heavy-duty hole punch or a disk cutter and then flattened as needed. A dual pulse shaper is shown mounted on the incident bar in Figure 31.
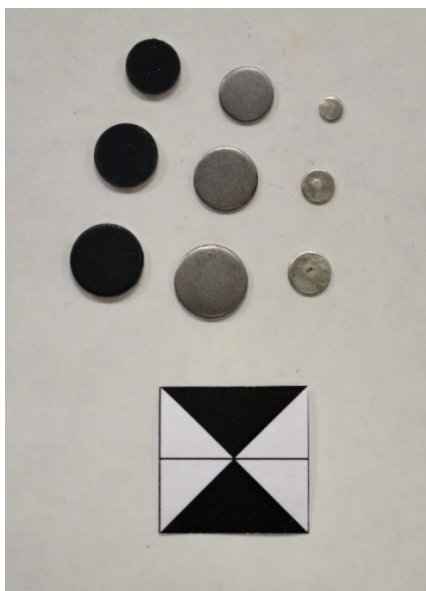
Figure 30. Various Sizes of Steel and Aluminum Pulse Shapers

Figure 31. Dual Pulse Shaper Installed on Incident Bar

The process for designing a pulse shaper utilized the recommendations from

Naghdabadi et al. Since the material being tested was known to have moderate to

high work hardening behavior, a relatively large pulse shaper was tried. Since the

slope of the work hardening phase in the first trial was too steep in relation to the

transmitted slope, shown in Figure 32, a larger diameter shaper was needed. In the

second attempt, shown in Figure 33, the slope of the incident wave is visibly lowered

from the first test. However, the slope of the transmitted wave also changed. This is

part of the difficulty of this type of test; the behavior of the test specimen cannot

always be predicted *a priori*.
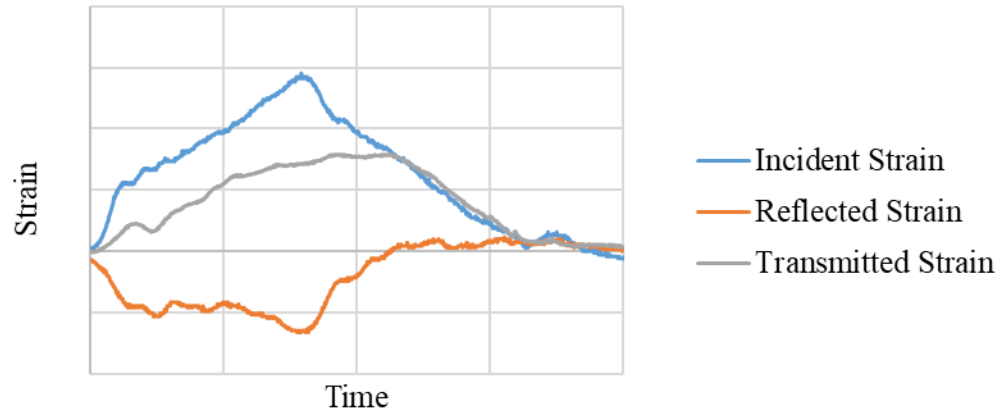
Figure 32. Initial Trial Showing Primary Pulse Shaper was too Small
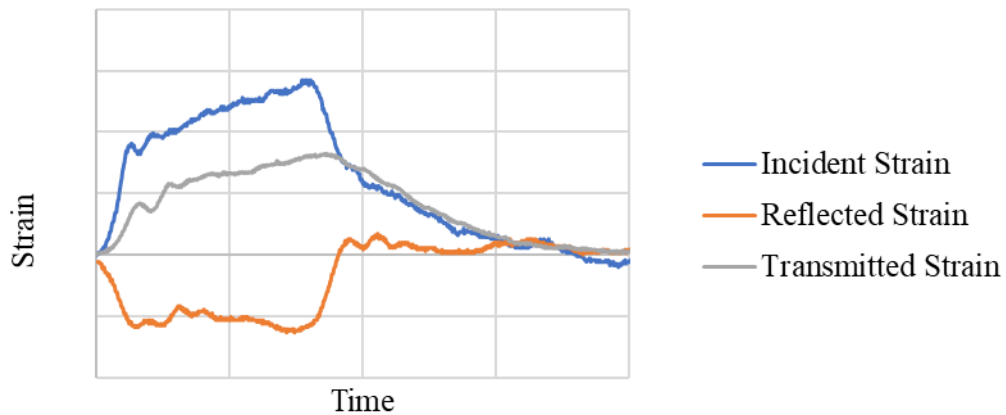
Figure 33. Subsequent Trial Showing Primary Shaper was still Too Small

The pulse shaper diameter was again increased and the results are shown in Figure 34. Note that the slope of the reflected wave is generally horizontal with some oscillations. The corresponding strain rate history is shown in Figure 35. Since the shape of the incident wave could not be directly matched to the transmitted wave with a single pulse shaper, this was the starting point for adding a secondary pulse shaper. The incident wave generally had the right shape to give the desired effect, the goal of the secondary pulse shaper was to damp out the high frequency oscillations with minimal changes to the overall shape.

47
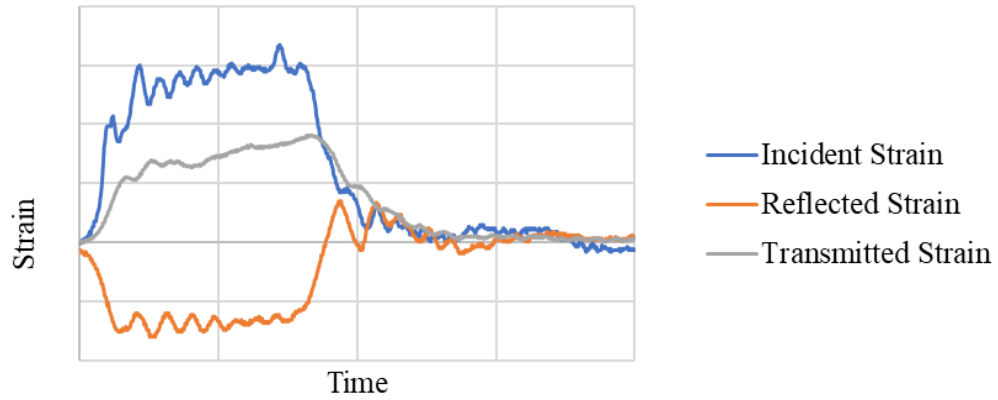
Figure 34. Trial Showing Primary Shaper was Adequate Size
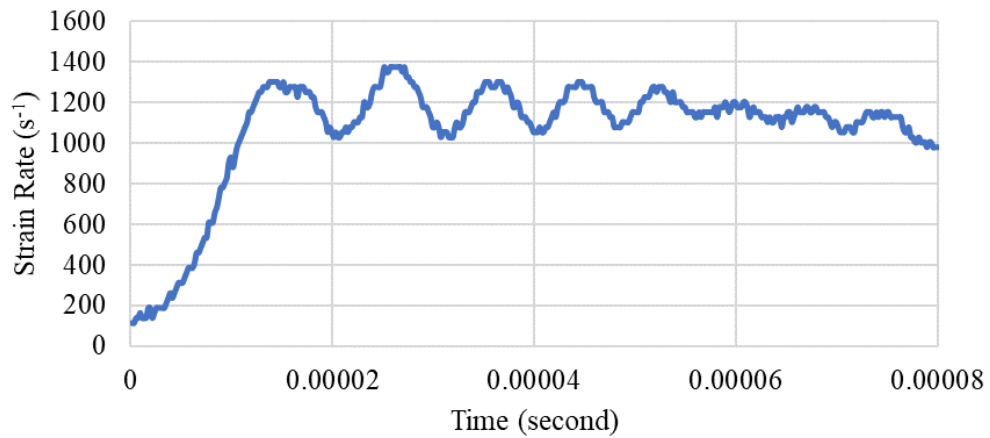
Figure 35. Strain Rate Profile with Adequate Size Primary Pulse Shaper

The guidelines for secondary pulse shaping are similar to single pulse shaping. If the slope of the incident pulse it too steep, a thicker or larger diameter secondary shaper is needed. When the slope is too flat, a thinner or smaller diameter shaper is needed. Figure 36 shows the strain rate improvement over Figure 35 when a secondary shaper was added.

48
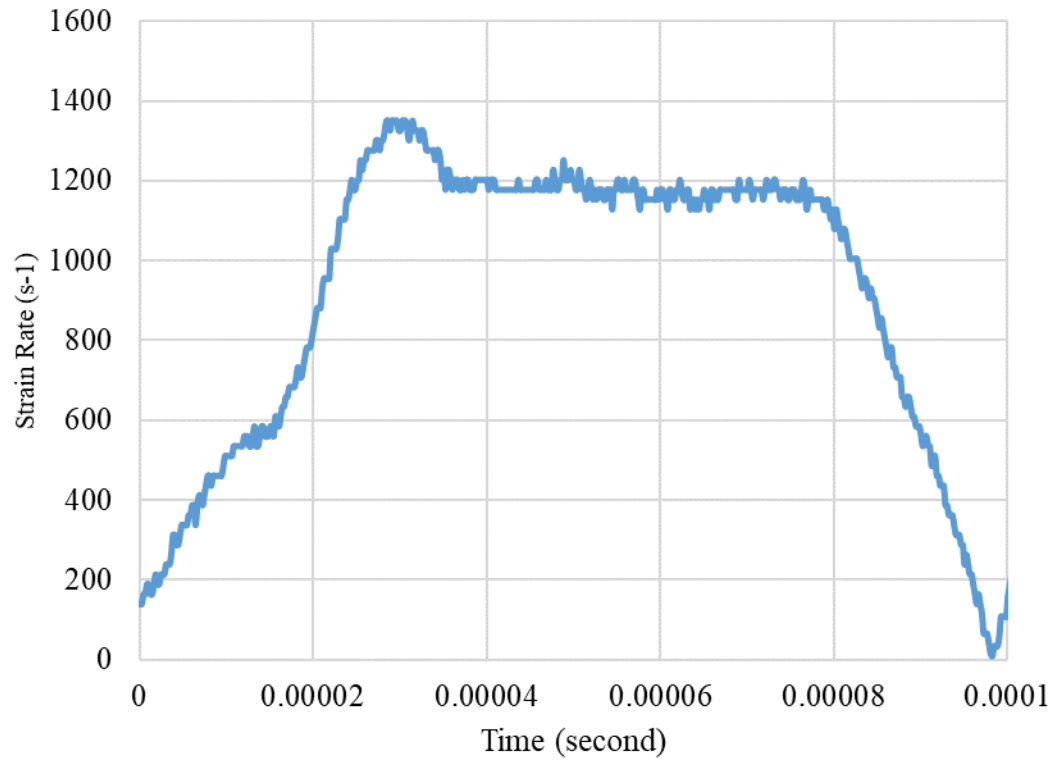
Figure 36.   Strain Rate from Dual Pulse Shaped Test

Chapter 6: Experimental Results

Tensile Tests

The six tested AM test samples shown in Figure 37, three printed in each direction, while somewhat ductile, did not show signs of necking during the testing process and they had a rough, porous looking fracture surface as shown in Figure 38. Additionally, there was significant differences in the rupture location and morphology between the build directions. The three horizontally printed samples tended to break in the middle of the gage section with the break occurring along a shear plane. The three vertically printed samples tended to break near the end of gage section with the rupture occurring along build layers. Overall, the elongation at breakage of the AM samples was 30-70% less than the values reported by the manufacturer.
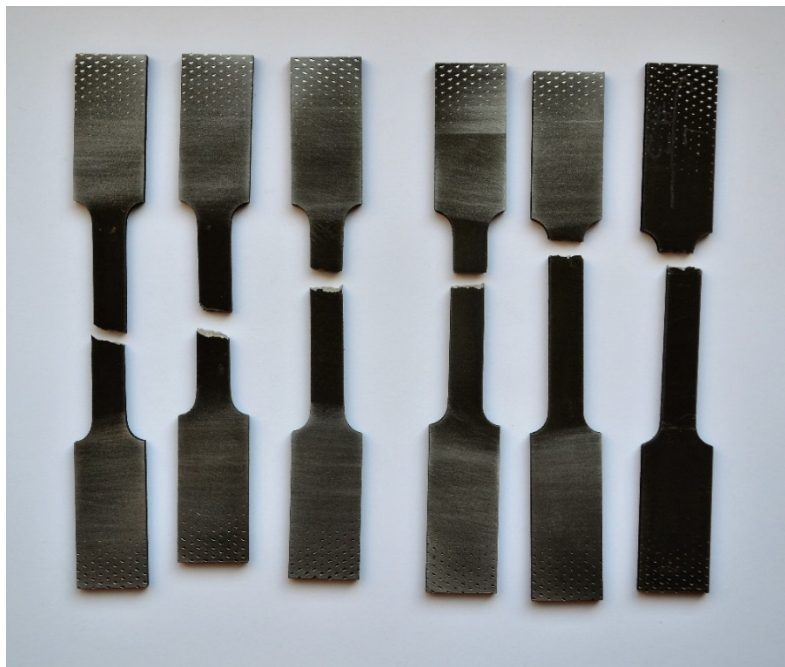
Figure 37. Additively Manufactured Tension Samples after Testing: (a) three horizontally printed, (b) three vertically printed
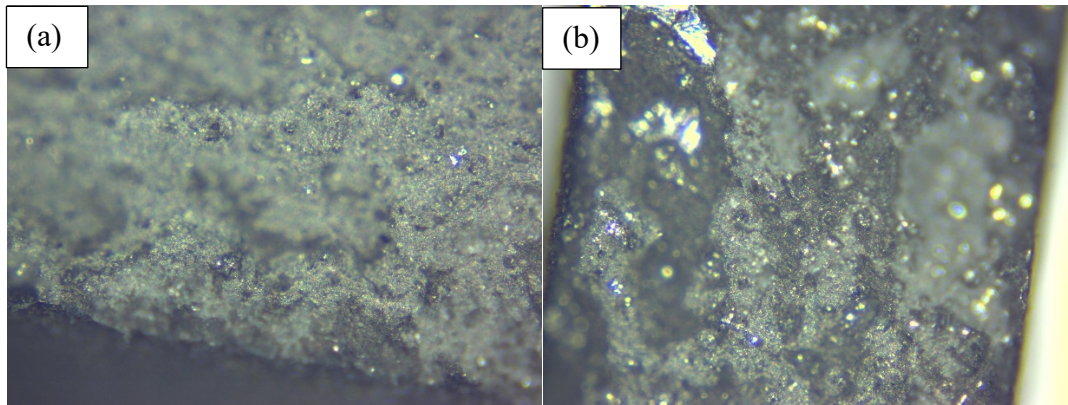
**Figure 38. Fracture Surfaces of Additively Manufactured Tensile Samples:
(a) horizontally printed (50x), (b) vertically printed (50x)**

The two wrought tensile samples, shown in Figure 39, clearly showed necking near the rupture site with cup and cone behavior typical of ductile fracture. The fracture surface is shown in Figure 40. The UTS and the elongation at breakage are comparable to the values reported by ASM International [23]. The plots of the eight tensile tests are shown in Figure 41 and the results of the tensile tests are summarized in Tables 6, 7, and 8. As expected, the AM specimens showed anisotropy of about 10% and the wrought material exhibited much more ductility than the AM specimens. Overall, the UTS and yield strength of all samples was comparable to literature values, while the elongation at breakage was significantly lower for the AM specimens.
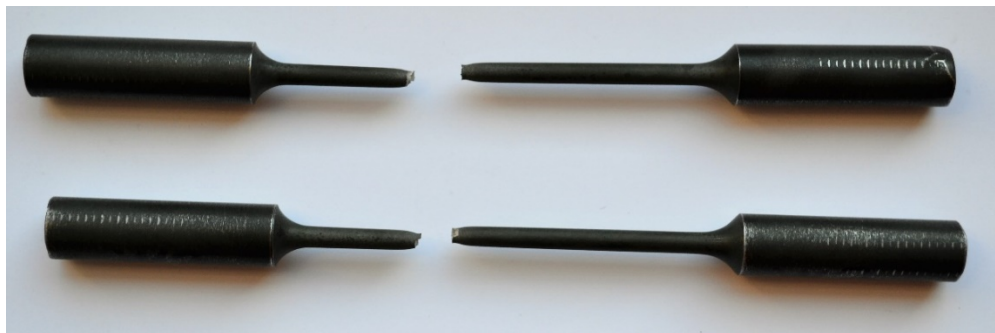
Figure 39. Wrought Tension Samples after Testing
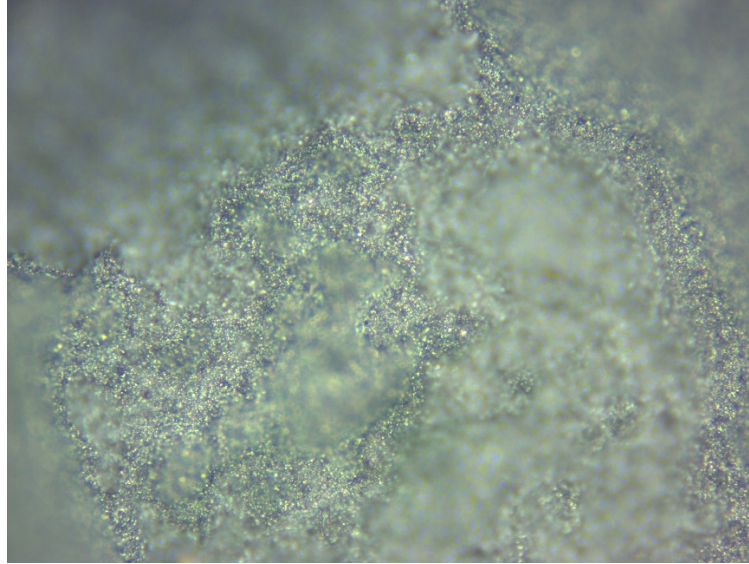
Figure 40. Fracture Surface of Wrought Tensile Sample (50x)
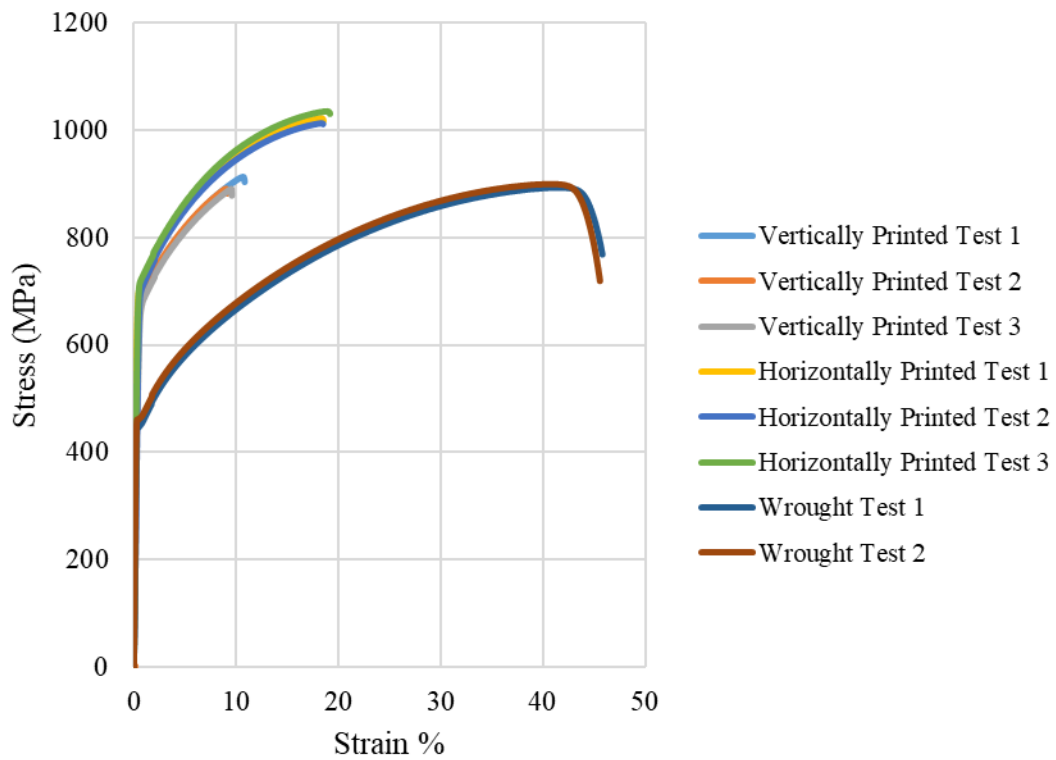
Figure 41. Stress Strain Curves of IN625 from Tensile Testing

Test Specimen Type	Average Yield Stress from Tensile Test (MPa)	Yield Stress from Literature (MPa)	Percent Difference
Wrought	454	490 [23]	-7%
AM Vertically Printed	680	600±20 [20]	+13%
AM Horizontally Printed	705	640±20 [20]	+10%

Table 6. Comparison of Tensile Yield Stress to Literature Values

Test Specimen Type	Average Ultimate Stress from Tensile Test (MPa)	Ultimate Tensile Stress from Literature (MPa)	Percent Difference
Wrought	897	965 [23]	-7%
AM Vertically Printed	899	980±20 [20]	-8%
AM Horizontally Printed	1020	1030±20 [20]	-1%

Table 7. Comparison of Tensile Ultimate Stress to Literature Values

Test Specimen Type	Average Elongation at Break from Tensile Test	Elongation at Break from Literature	Percent Difference
Wrought	46%	50% [23]	-8%
AM Vertically Printed	9.8%	34±3% [20]	-70%
AM Horizontally Printed	18.7%	27±3% [20]	-30%

Table 8. Comparison of Elongation at Break to Literature Values

Compression Tests

Out of 35 tests, 10 provided usable results and few provided very good results. This shows the relative difficulty in finding a good pulse shaper design. The results of the high strain rate compression tests are summarized in Figure 42. There are significantly different curves for the additive and wrought materials which is consistent with the tensile tests. Both the yield stress and the strain hardening rates between the two material types are significantly different. The difference of the stress strain curves for the two AM print directions, if it exists, is much less pronounced than that the tensile tests. None of the compressive test materials show significant strain rate effects, as many of the stress strain curves from tests conducted at different strain rates lie on top of each other.

Determining the yield point of high strain rate compressive tests is a challenge. Since the stress in the sample does not reach instantaneous equilibrium, the stress strain curve does not have a smooth transition from elastic to plastic and therefore the Kolsky bar is not good for accurately determining the elastic portion of the stress strain curve [3]. However, using a linear regression the yield stresses can be approximated and are shown in Table 9. These values are consistent with the yield stress found during the tensile tests. Figure 43 shows the yield stress vs strain rate for IN625. The results of the tests confirm that there is minimal strain rate effect on the yield stress.
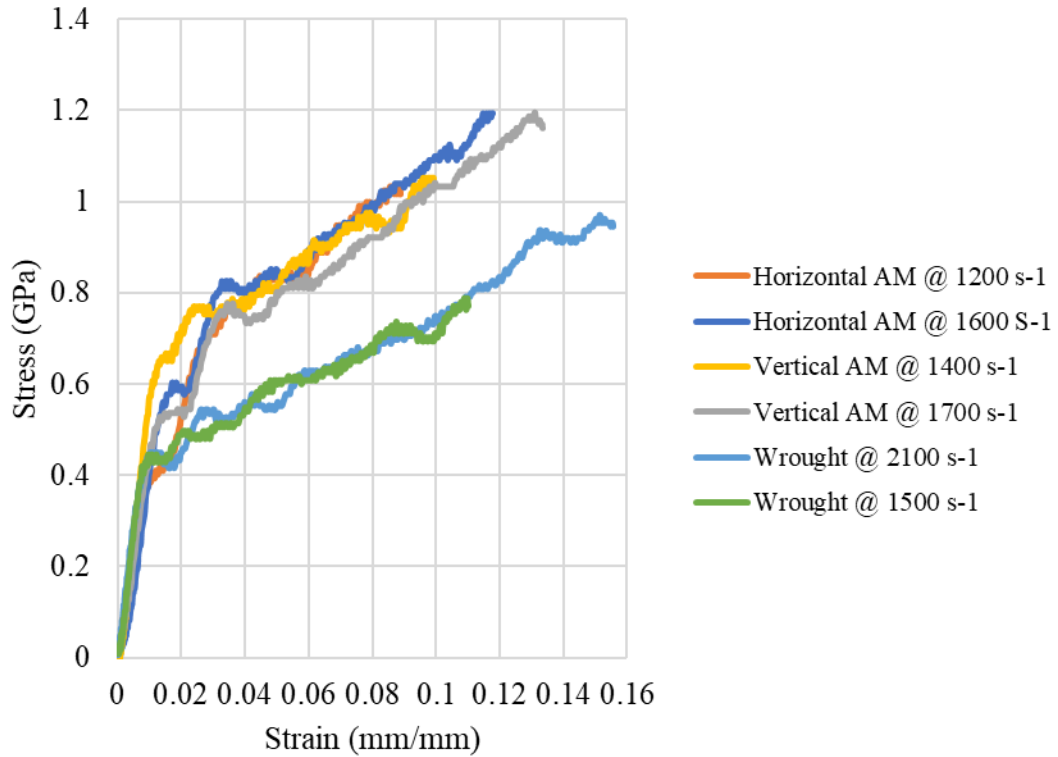
Figure 42. Compressive Stress Strain Curves of IN625 from High Strain Rate Testing

Material Properties	AM Vertically Printed	AM Horizontally Printed	Wrought
Approximate Yield Stress (MPa)	600-650	650-700	400-450
Approximate Difference of Yield Stress from Tensile Tests	-7%	-3%	-5%
Strain Hardening Slope (MPa/strain)	44	48	34

Table 9. Summary of High Strain Rate Compressive Test Results
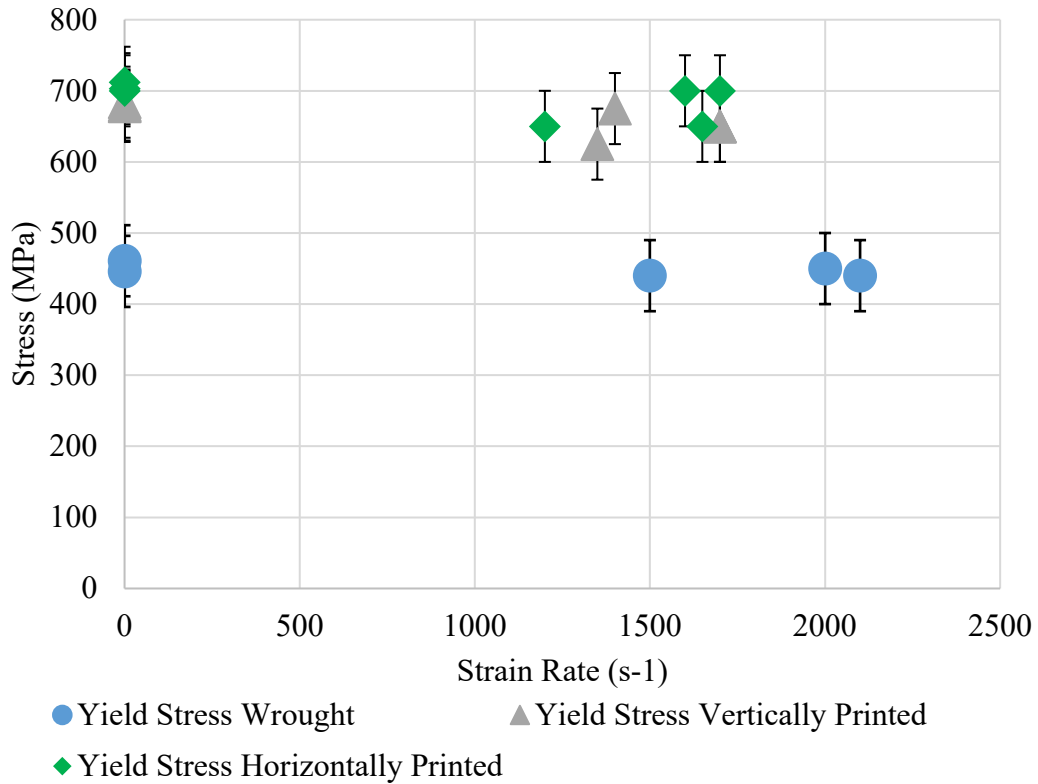
Figure 43. Yield Stress vs Strain Rate

Discussion

First, I would like to discuss possible sources of error within the experiment and then I would like to suggest ways to improve the capability of the testing apparatus. There are several known sources for error during Kolsky bar testing. Kariem et al (2012) discussed the importance of bar alignment on test accuracy [27]. The bars may be misaligned in six ways: neutral axis offset, uneven support height, non-parallel impact face, bar straightness, domed impact face, and cupped impact face. These misalignments all have a negative effect on signal accuracy. In this experiment five of the six alignment issues were mitigated while one, bar straightness, was known to be an issue and was managed as well as could be done.

56

An issue that may have helped improve repeatability was the consistency of the physical dimensions of the compression specimens. While the diameter of all specimens was easily controlled, the height of the specimens varied due to the machining and finishing of the ends of the specimen to make them flat.

I would have liked to achieve a higher total strain during the compression testing but this proved to be beyond the capability of the equipment. It is easier to achieve a higher total strain by a longer pulse duration, i.e. using a longer projectile, than by hitting the sample harder. Longer pulse duration gives the sample more time to deform and the sample will have more time under stress equilibrium. However, to use a longer striker would necessitate the use of a longer incident bar to avoid the incident and reflected signals from overlapping.

Additionally, it would have been ideal to get a larger spread on the strain rates for the compression testing. This proved to be a challenge. When the striker velocity was increased in an attempt to increase the strain rate, a larger pulse shaper was needed. The use of the larger pulse shaper then decreased the strain rate so that the total increase in strain rate was much less drastic.

Lastly, it would have been idea to use identical geometries for the wrought and AM tension samples. Round bar stock proved to be the easiest to source and machine for the wrought material. The AM sample geometry was selected due to the limitations of the 3D printer. First, printing tall thin objects can be a problem for LPBF printers so a geometry large enough to avoid warping was chosen. Second, since the specimens were of a very short length it was deemed important to maximize the grip

surface to reduce the chance of slipping. Due to these reasons two different

geometries were used.

Conclusion

The ultimate strength and yield strength of the tensile samples was within 13% of

published values. The AM samples showed an anisotropy in yield and ultimate

strength of up to 10% which is consistent with the expected behavior of AM metals.

However, the elongation of the samples 30-70% less than the values claimed by the

manufacturer. This could be a result of the print quality, annealing protocol of the

test samples, or sample geometry.

The results of the stress strain curves of the compressive tests showed significantly

different properties for wrought and AM IN625. The AM material had higher yield

stress and an showed a slightly faster strain hardening response when compared to

wrought material. There did not seem to be a significant difference in compressive

properties between the two directions of AM IN625. Additionally, there did not

appear to be any significant strain rate sensitivity.

Appendices

Compression Test Data

Horizontally Printed IN625 Tested at 1200 s^{-1} (Test Number HA11)
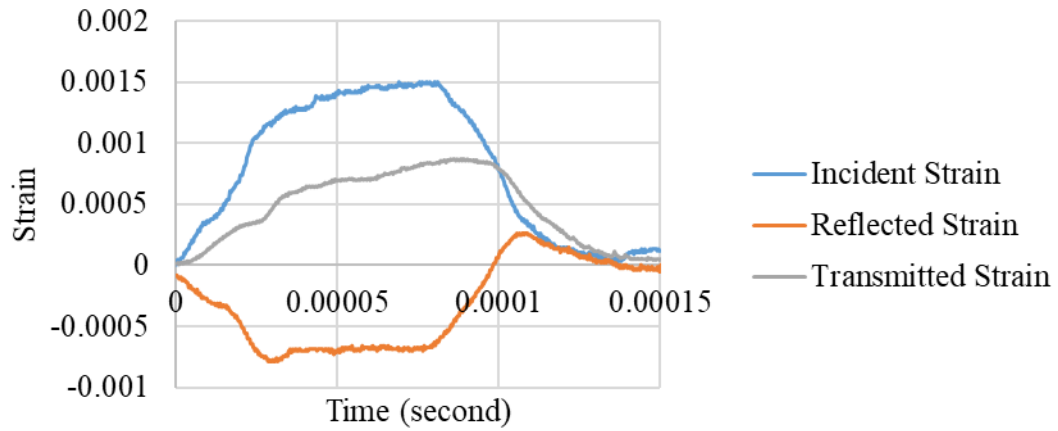
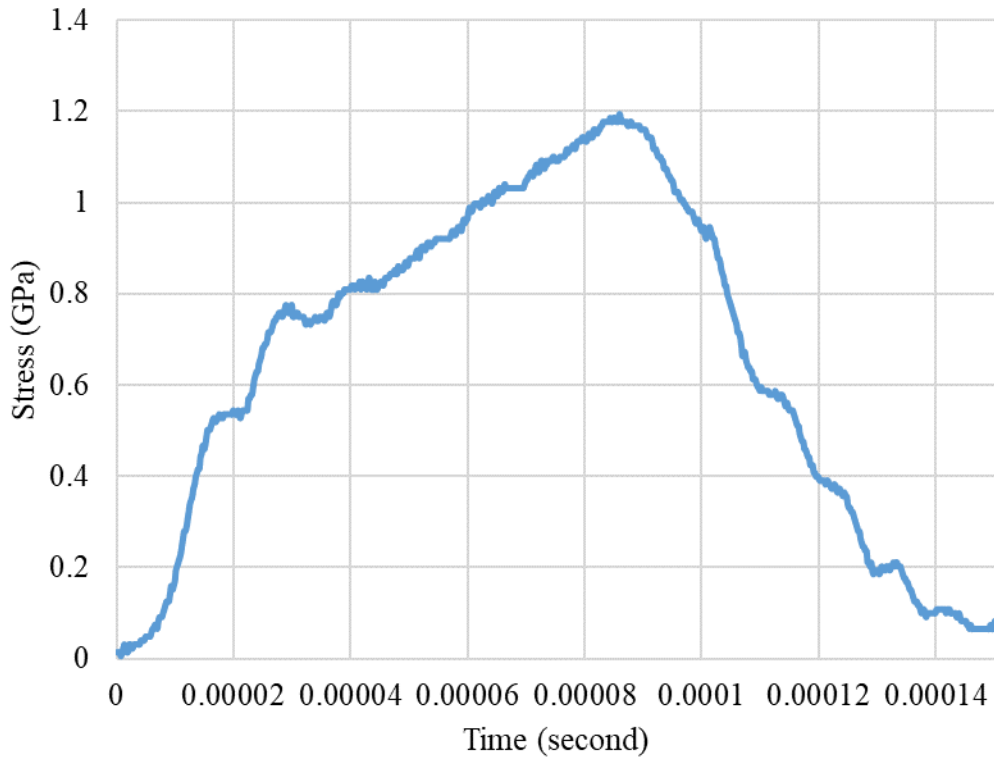**Figure A1. Aligned Compression Test Signals**
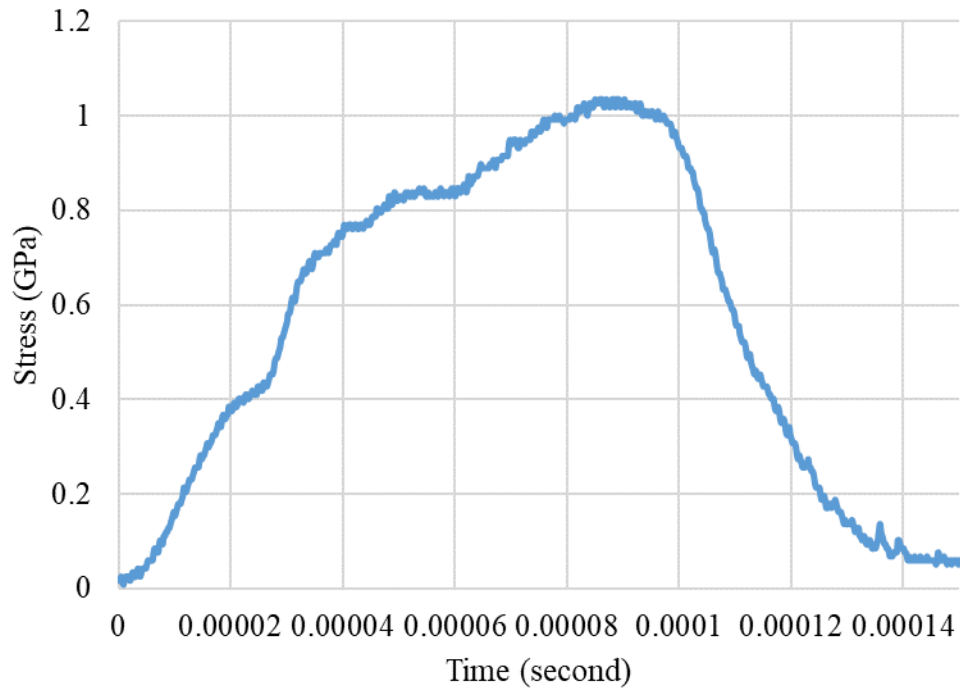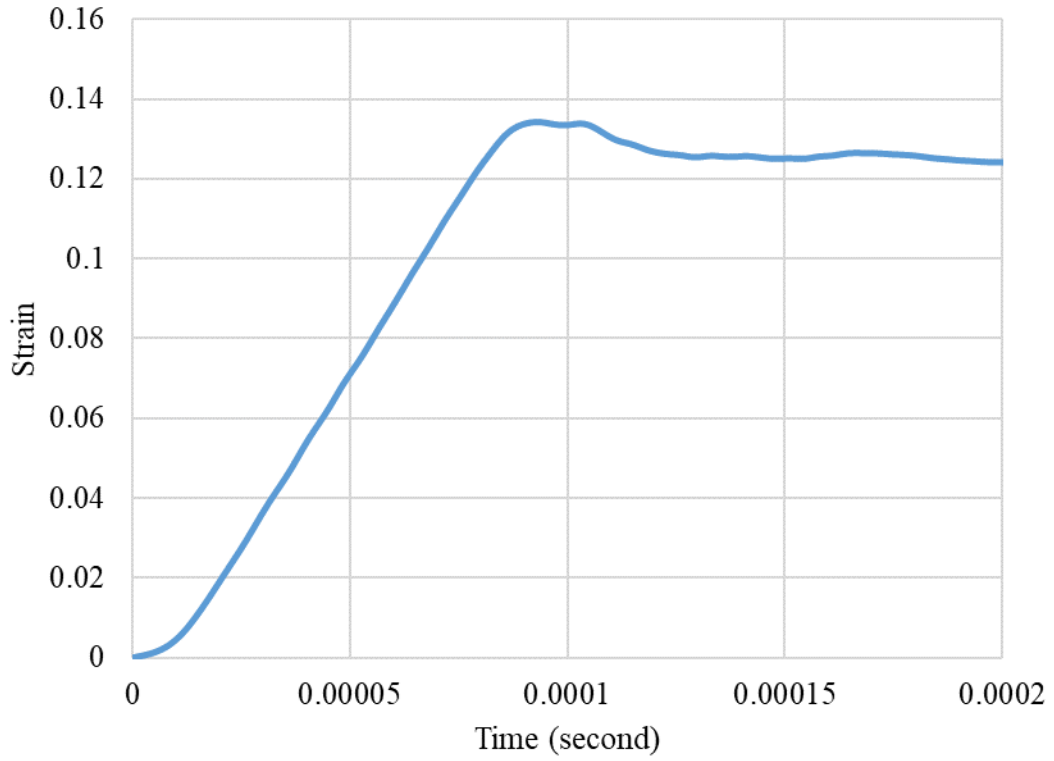

Figure A2. Sample Stress vs Time
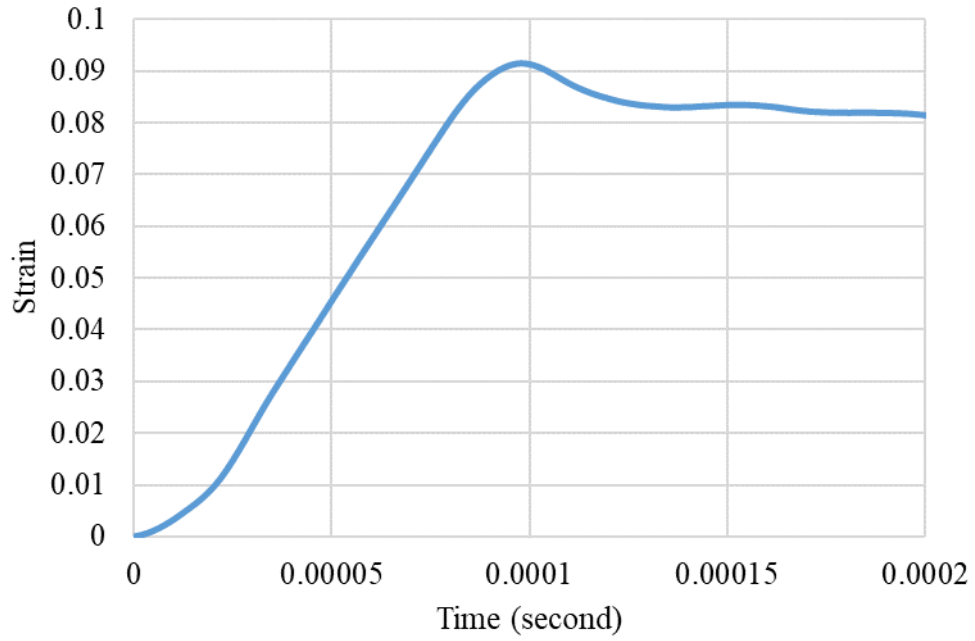
Figure A3. Sample Strain vs Time
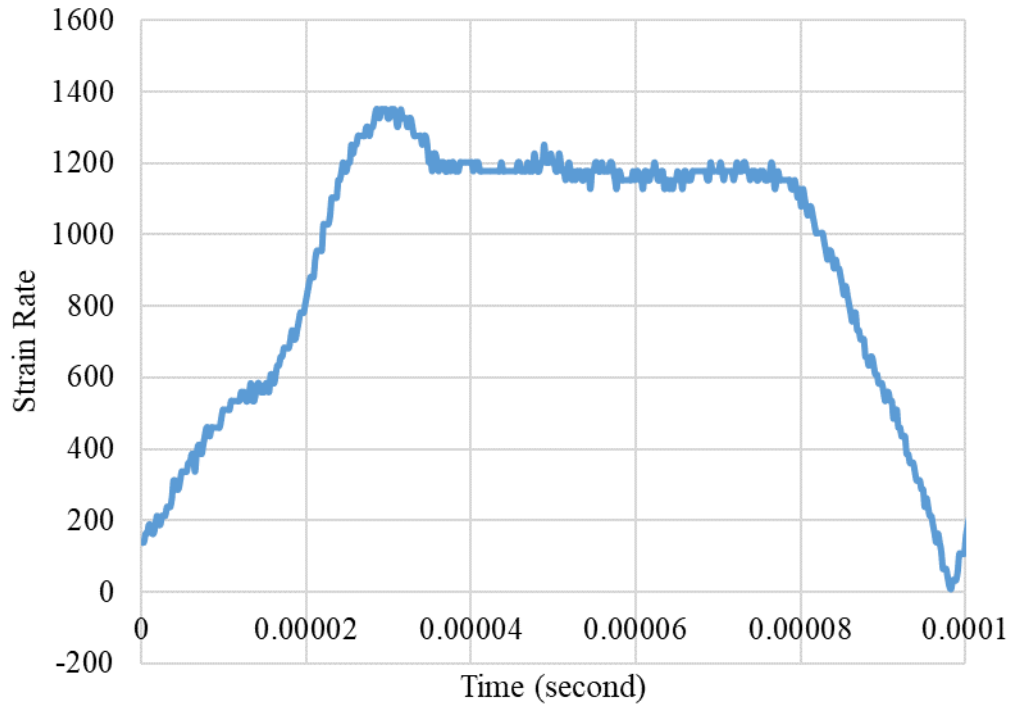
Figure A4. Sample Strain Rate vs Time
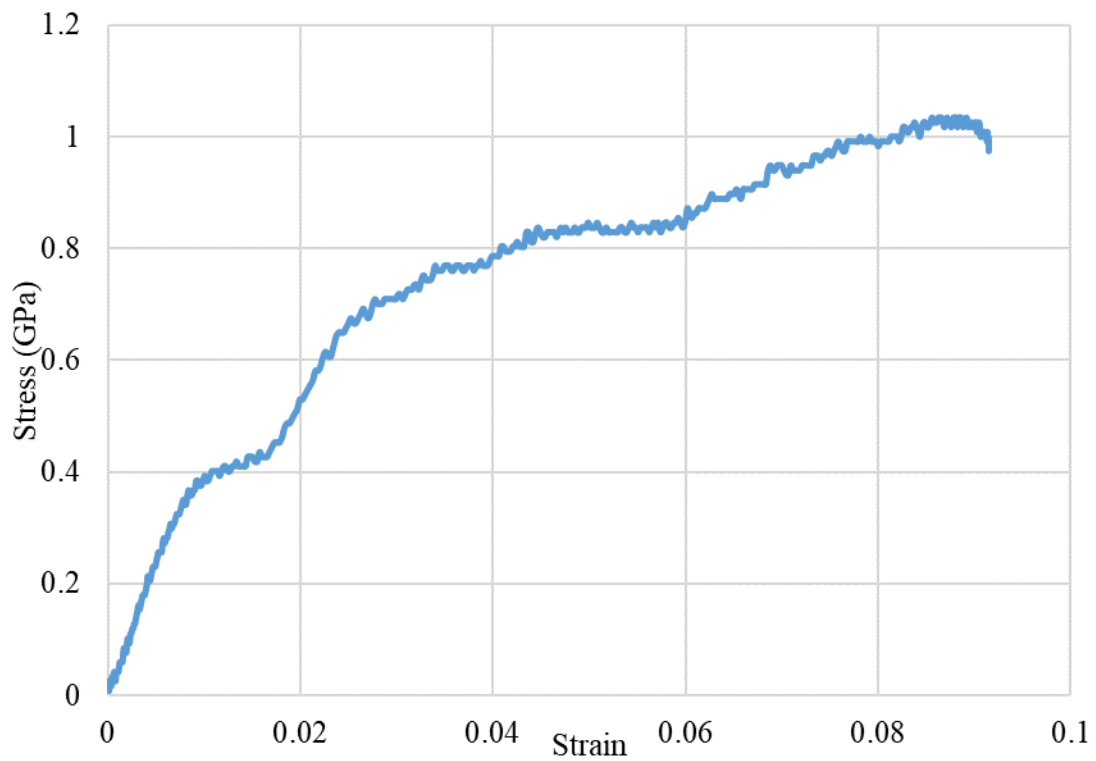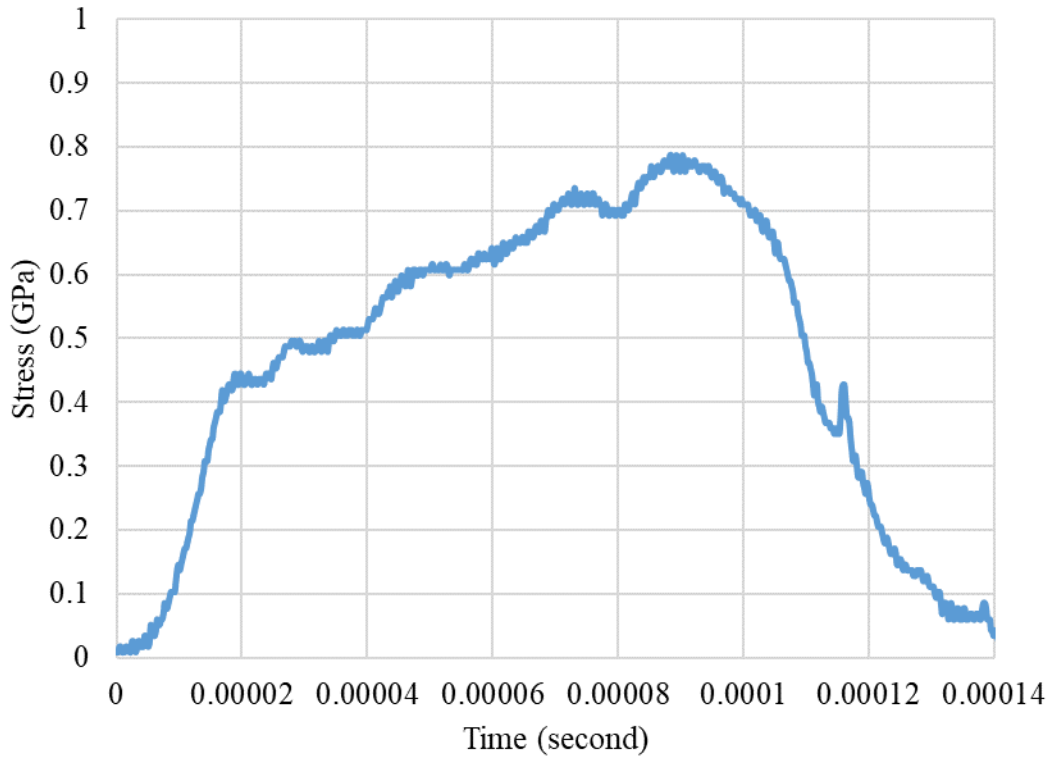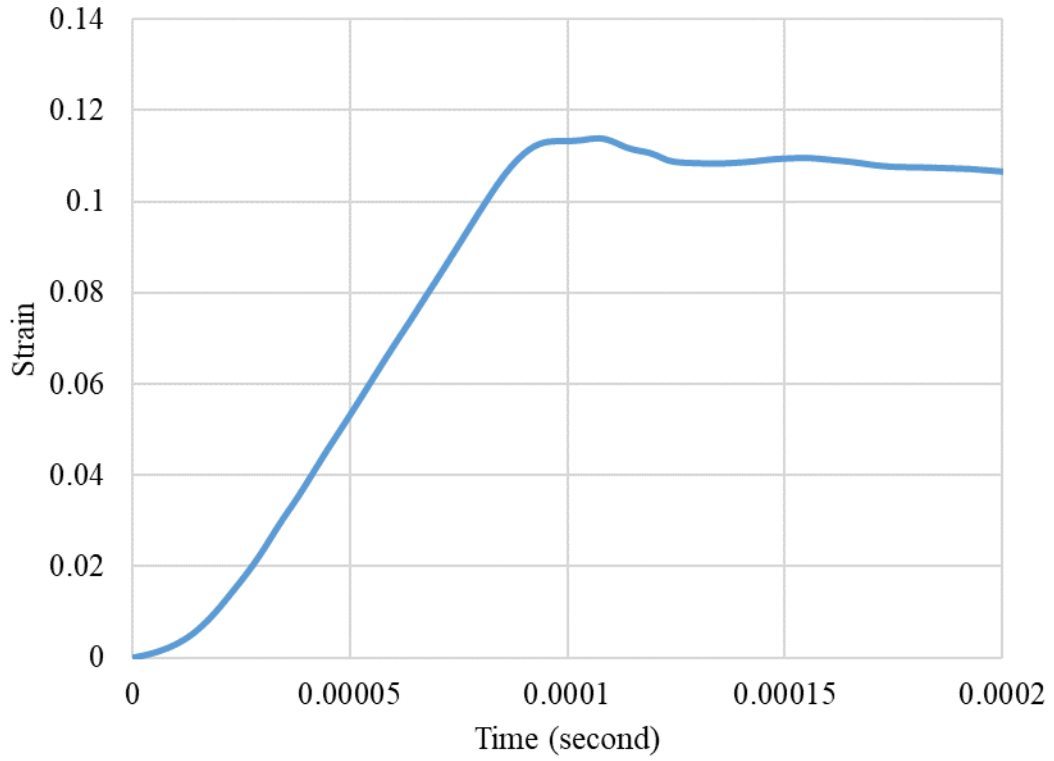
Figure A5. Sample Stress vs Strain Curve
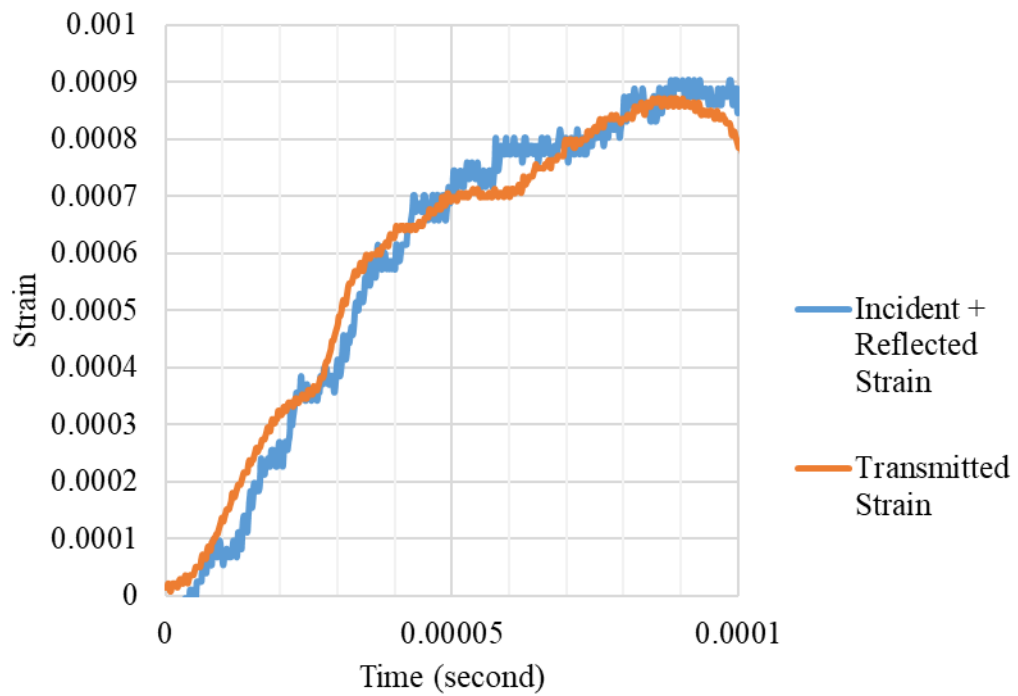
Figure A6. Sample Stress Equilibrium

Horizontally Printed IN625 Tested at 1600 s⁻¹ (Test Number HA4)
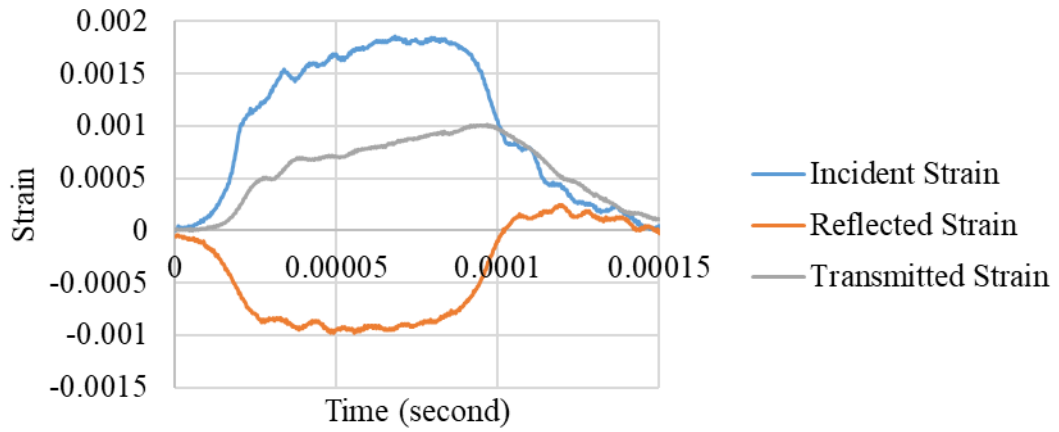
Figure A7. Aligned Test Signals
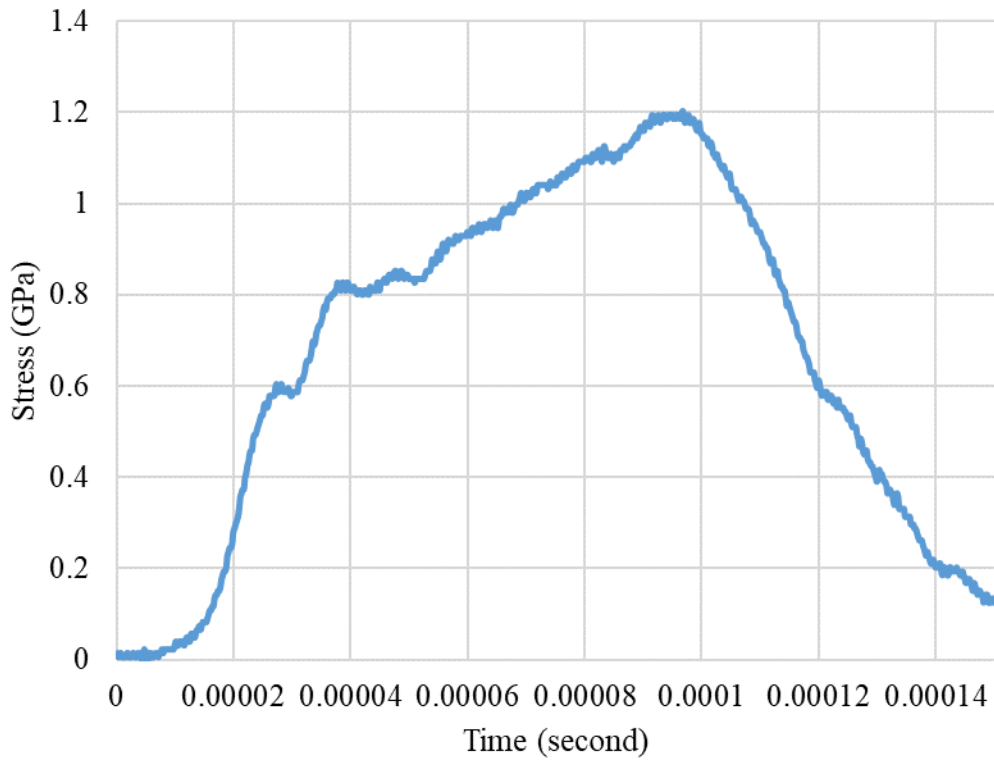
Figure A8. Sample Stress vs Time
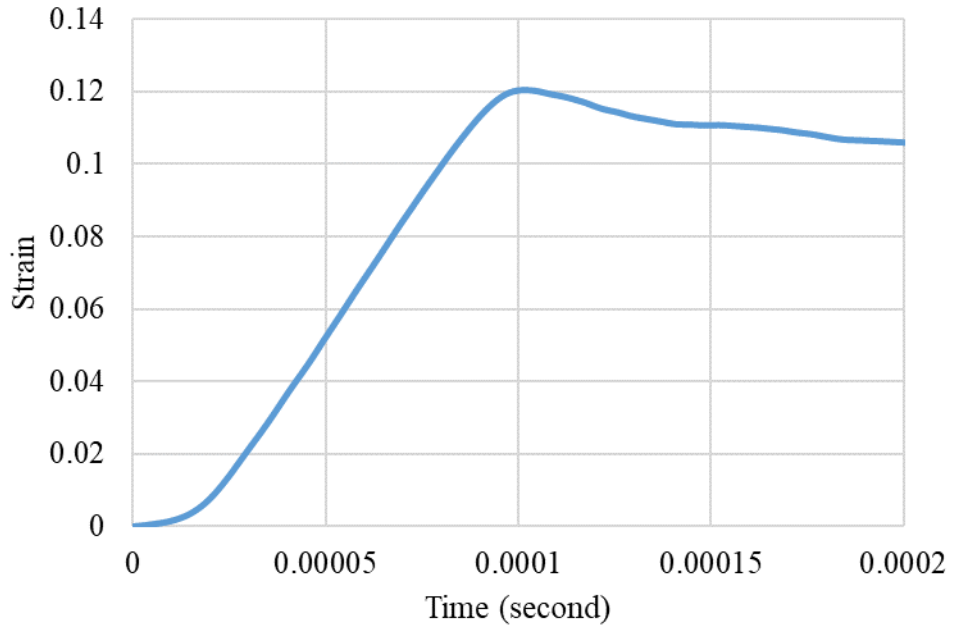
Figure A9. Sample Strain vs Time
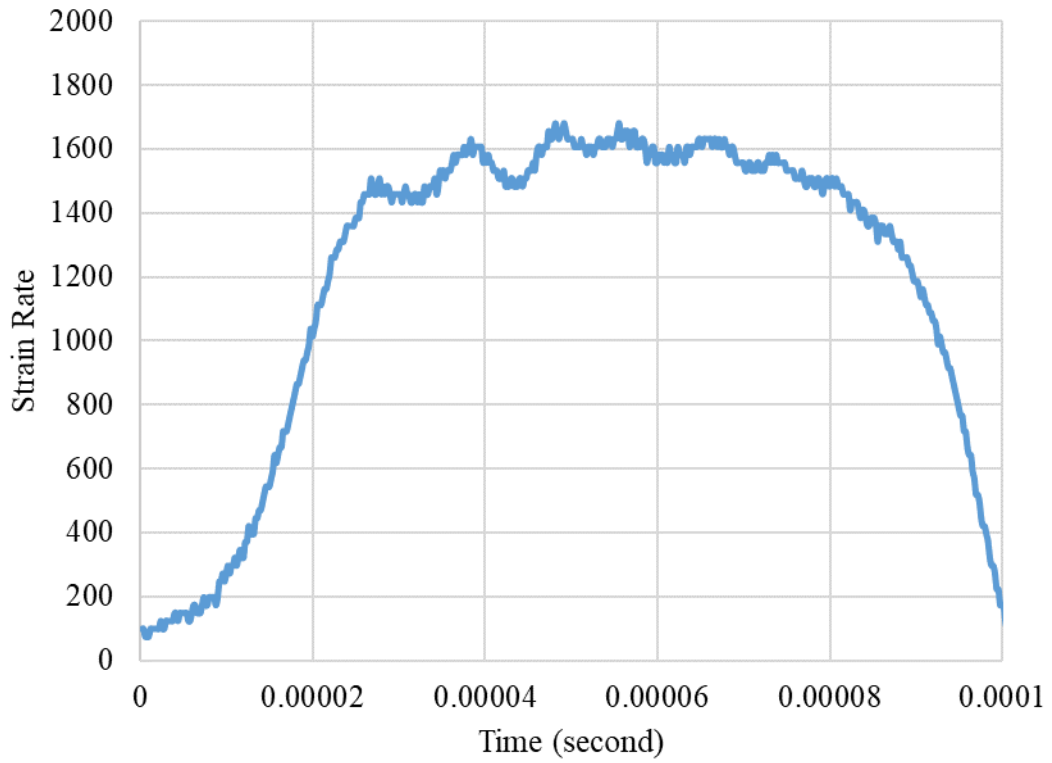
Figure A10. Sample Strain Rate vs Time
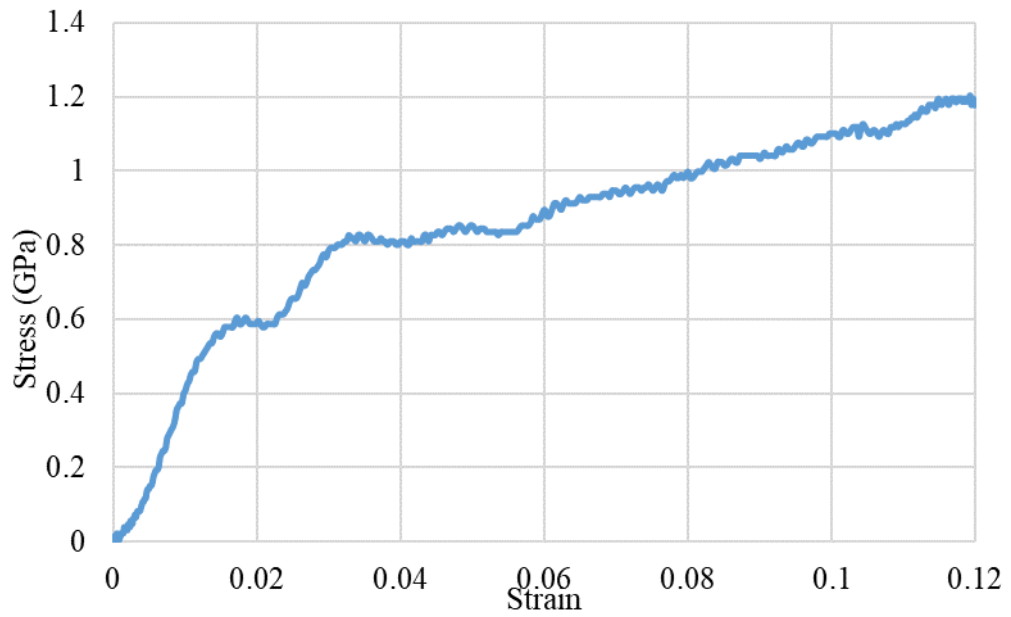
Figure A11. Sample Stress vs Strain Curve
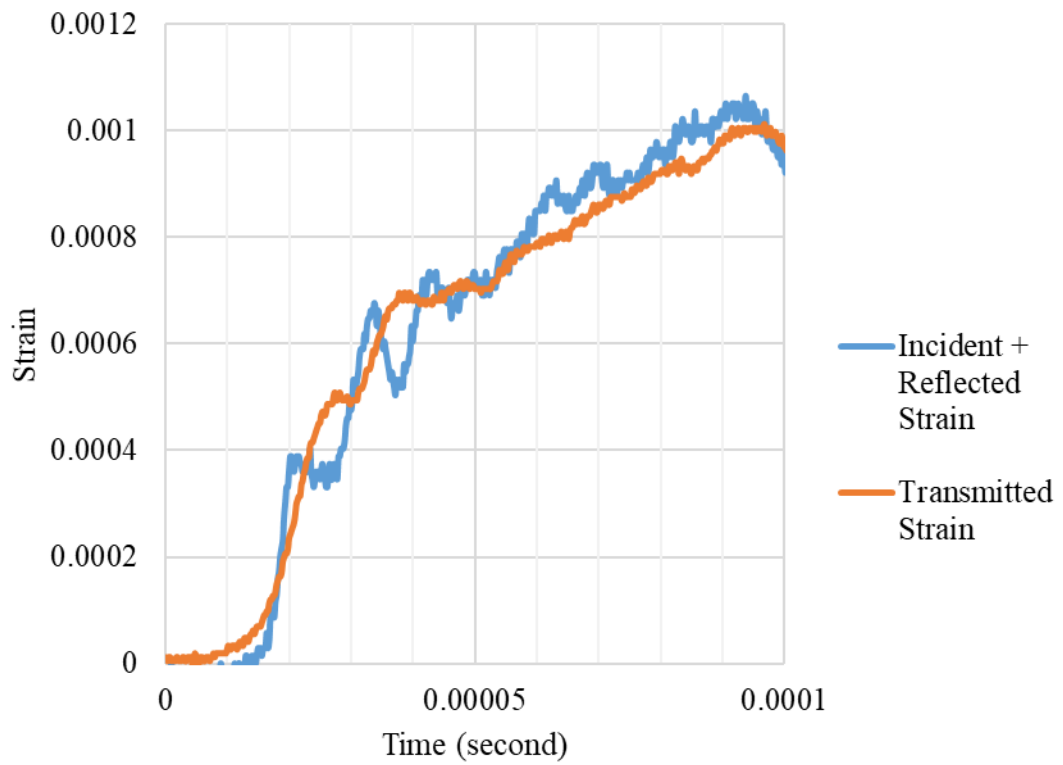
Figure A12. Sample Stress Equilibrium

Figure A13. Aligned Test Signals
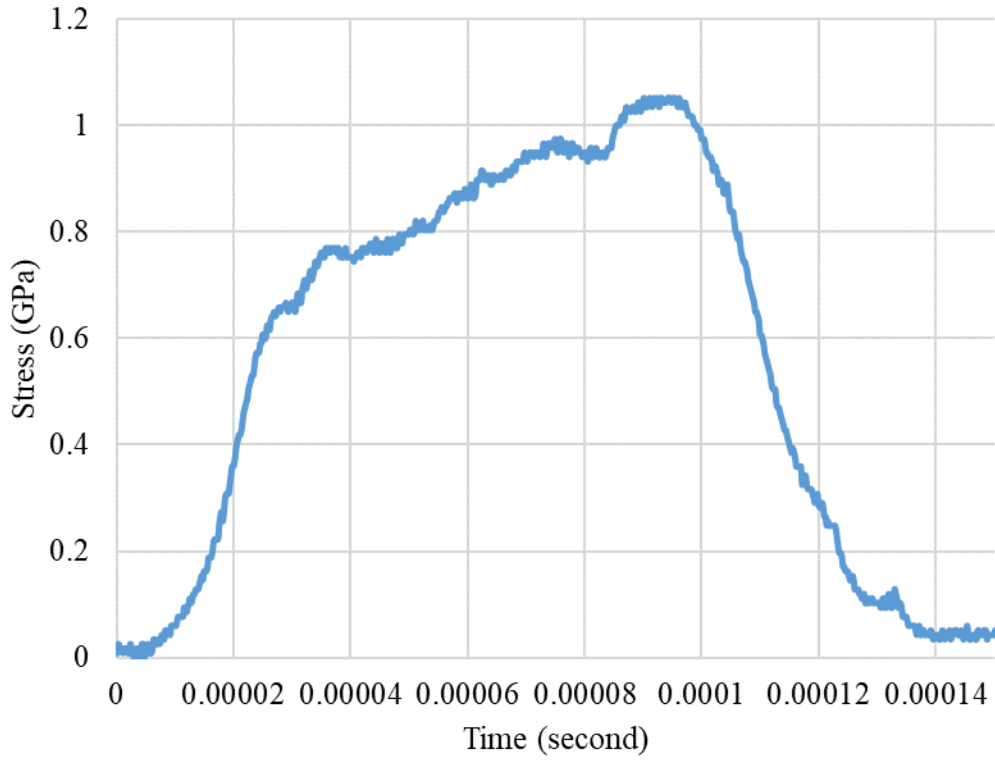
Figure A14. Sample Stress vs Time
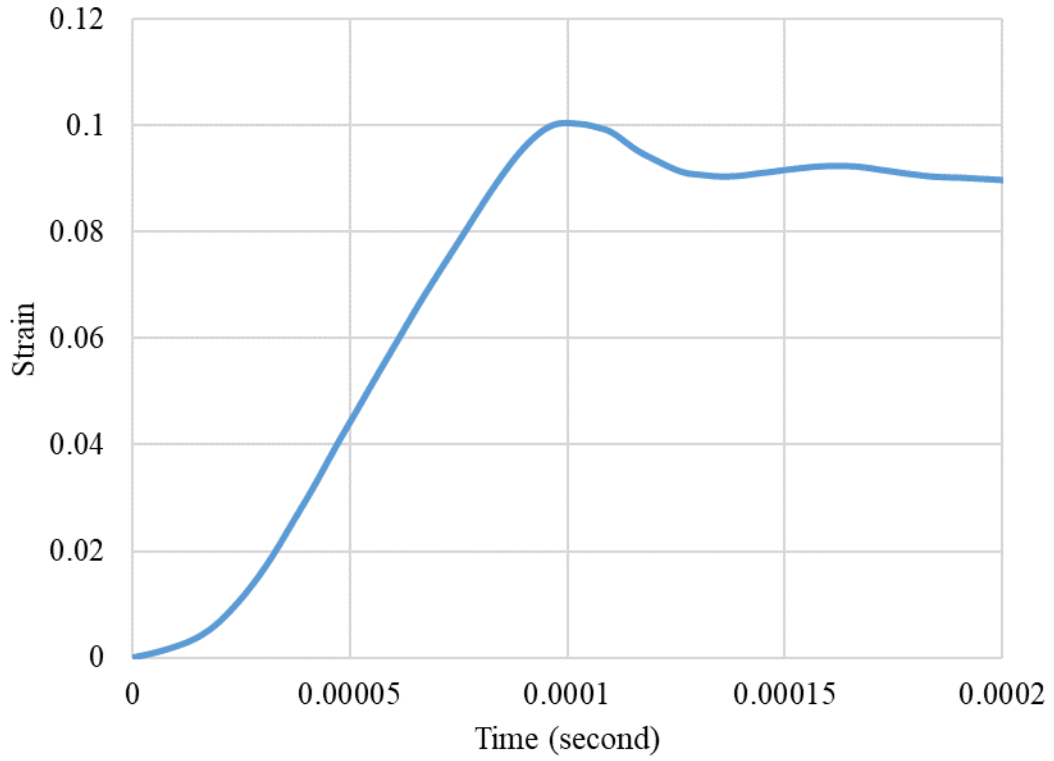
Figure A15. Sample Strain vs Time
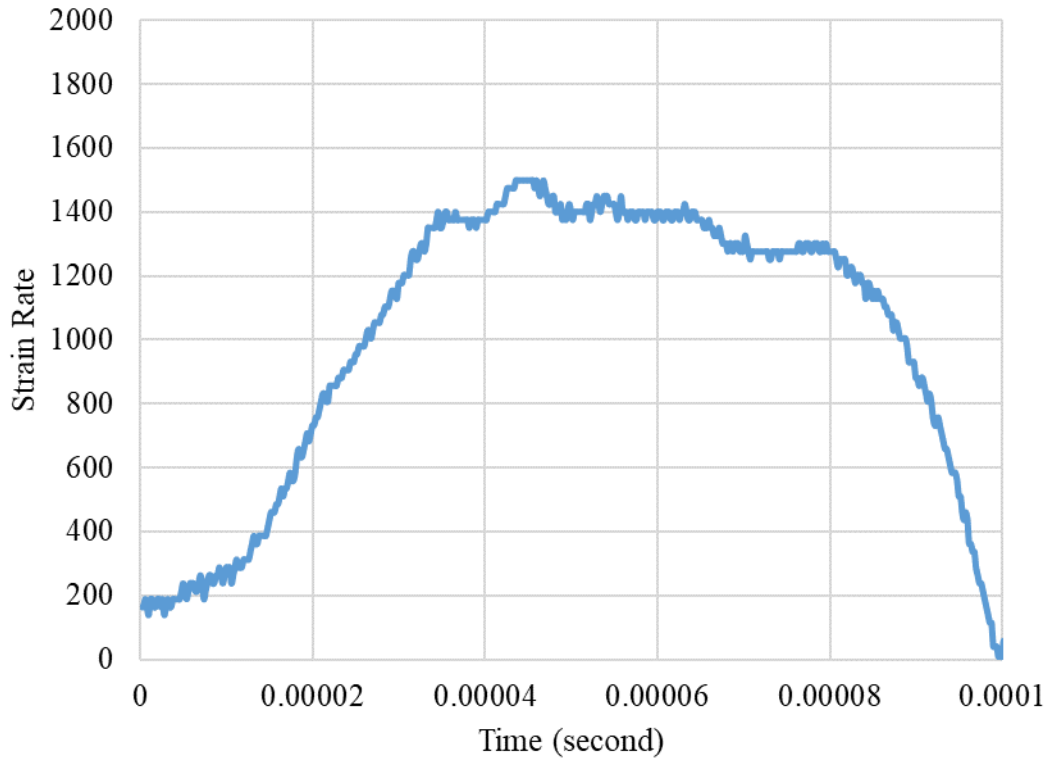
Figure A16. Sample Strain Rate vs Time
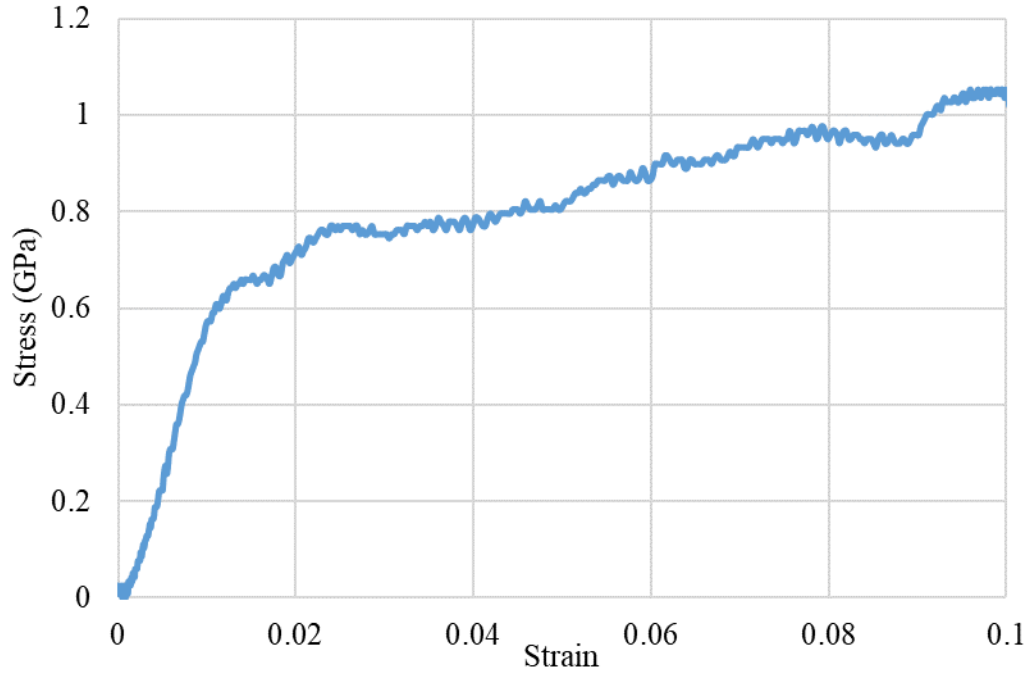
Figure A17. Sample Stress Strain Curve
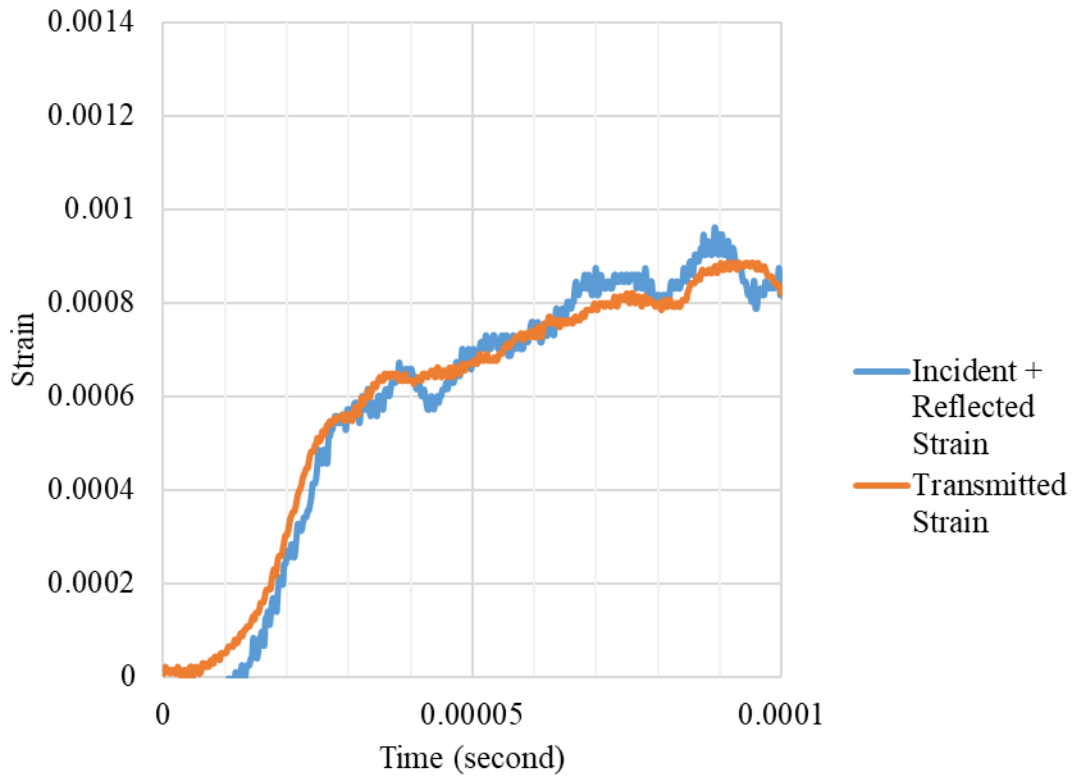
Figure A18. Sample Stress Equilibrium

Vertically Printed IN625 Tested at 1700 s^{-1} (Test Number VA7)
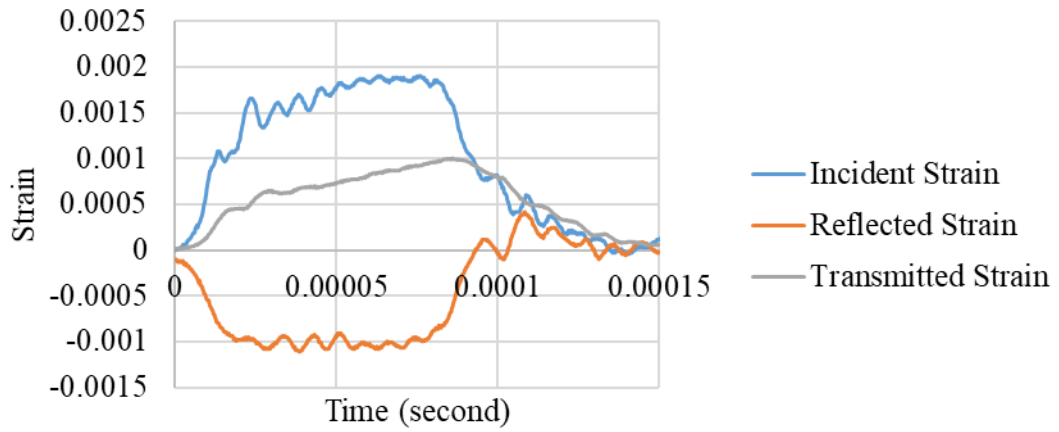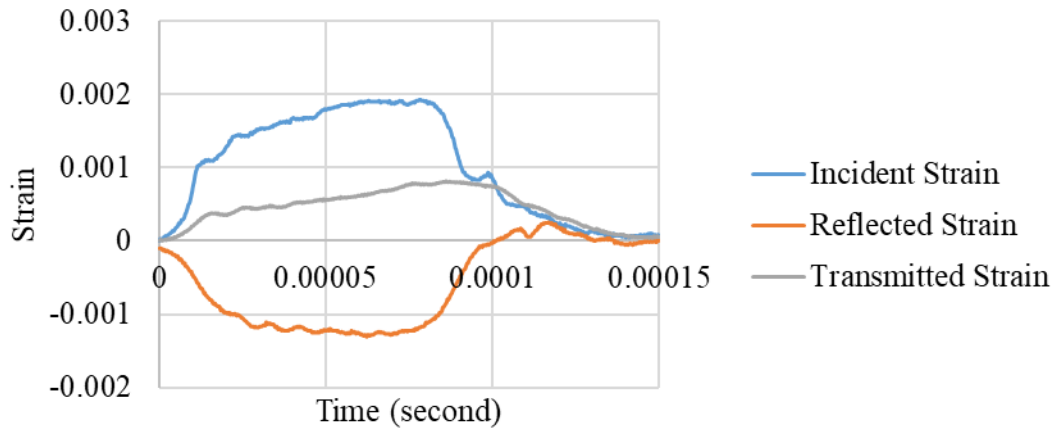

Figure A19. Aligned Test Signals

Figure A20. Sample Stress vs Time

Figure 21. Sample Strain vs Time
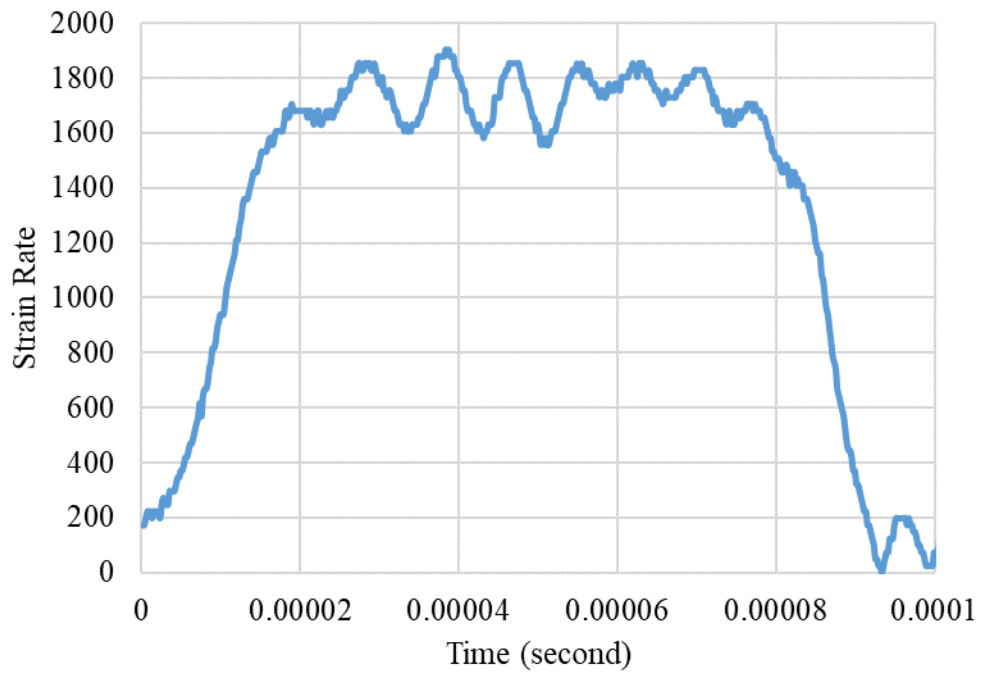
Figure A22. Sample Strain Rate vs Time
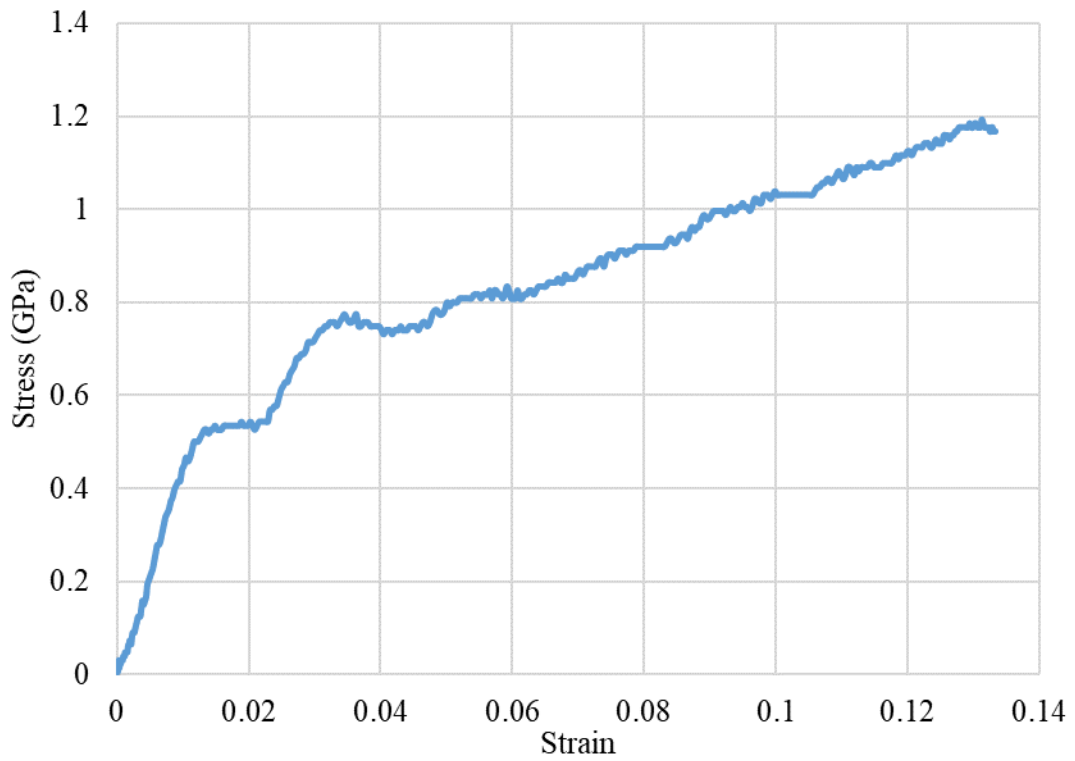
Figure A23. Sample Stress vs Strain Curve
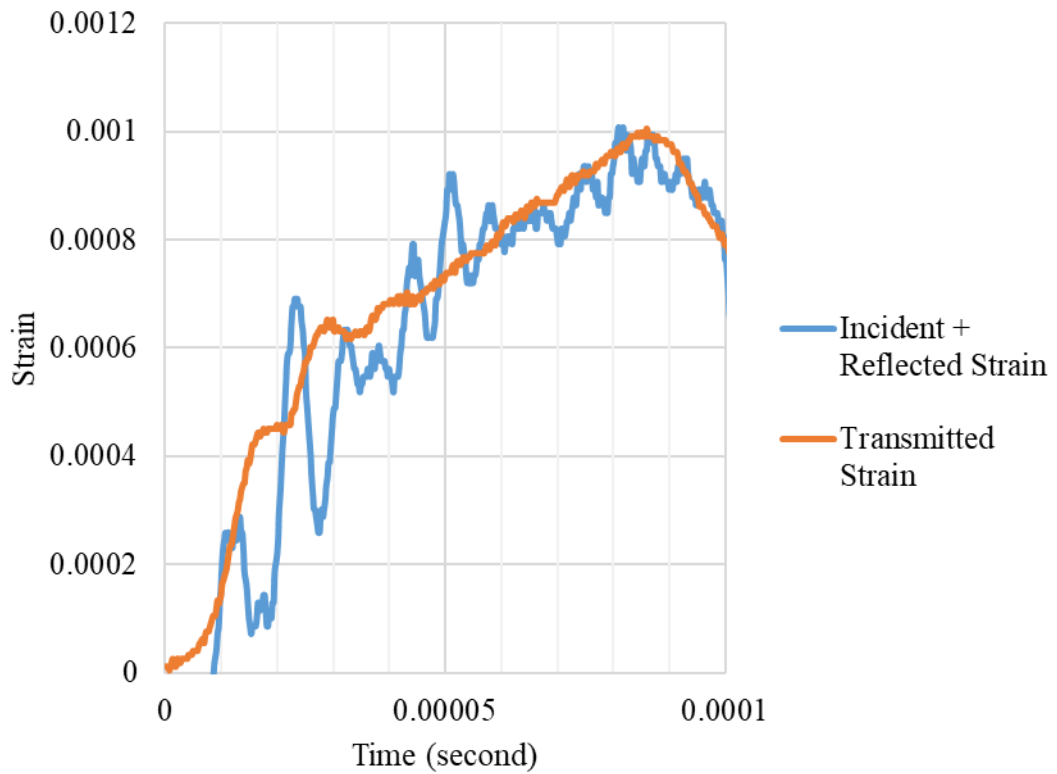
Figure A24. Sample Stress Equilibrium
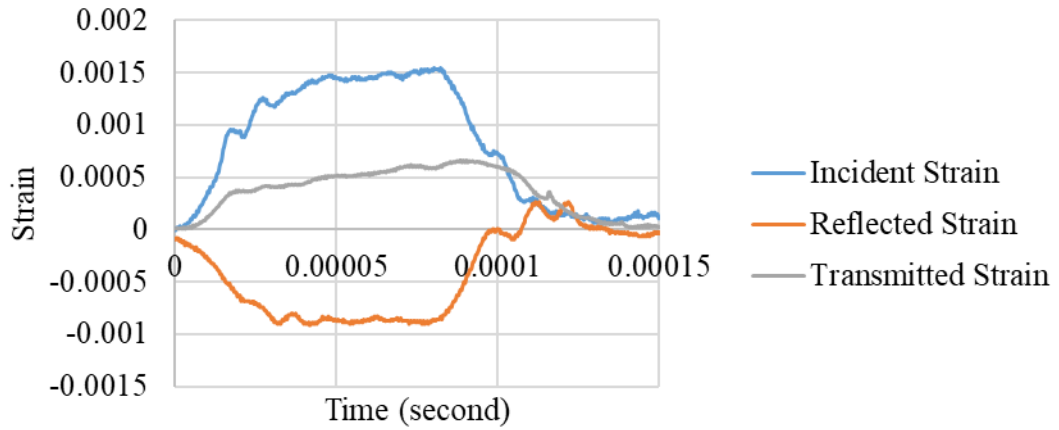
Figure A25. Aligned Test Signals

Figure A26. Sample Stress vs Time

Figure A27. Sample Strain vs Time
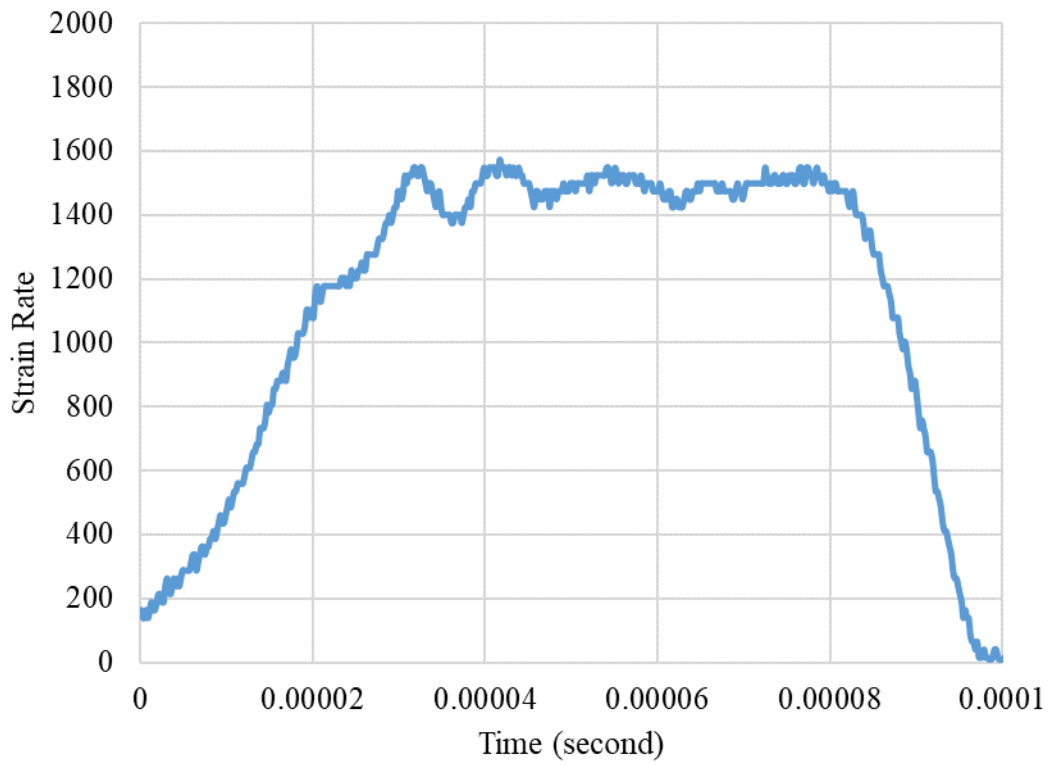
Figure A28. Sample Strain Rate vs Time

72
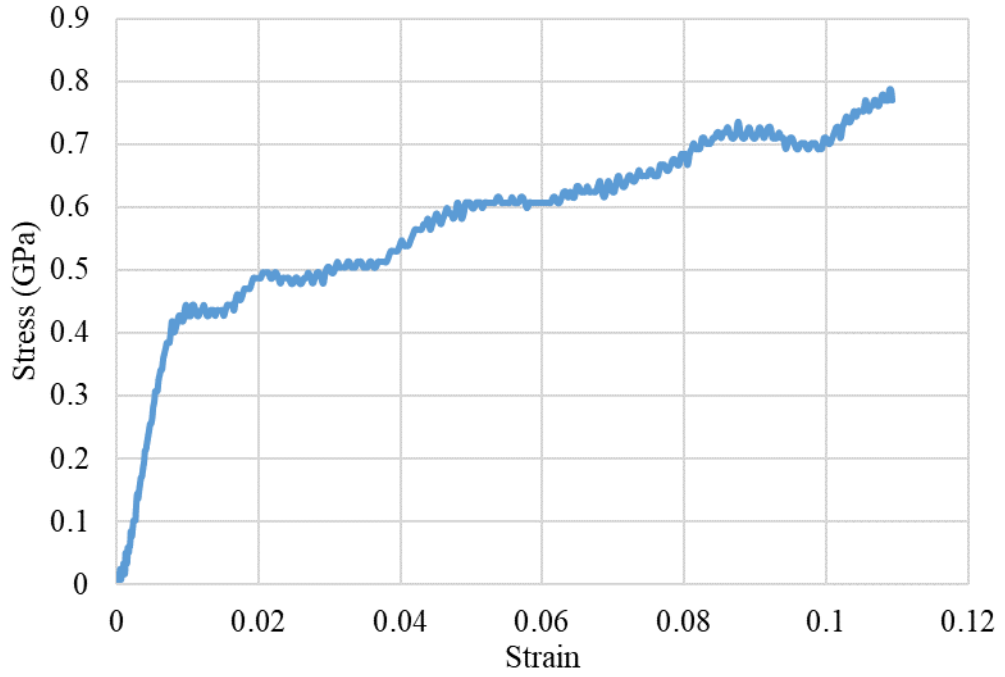
Figure A29. Sample Stress vs Strain Curve
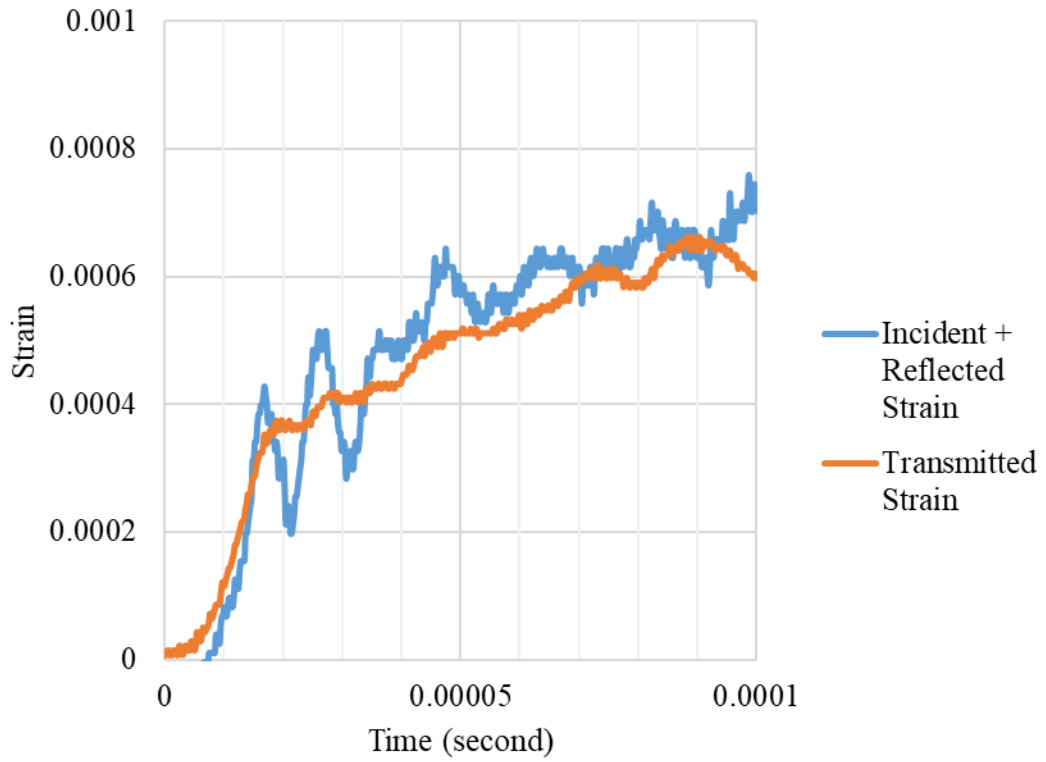
Figure A30. Sample Stress Equilibrium
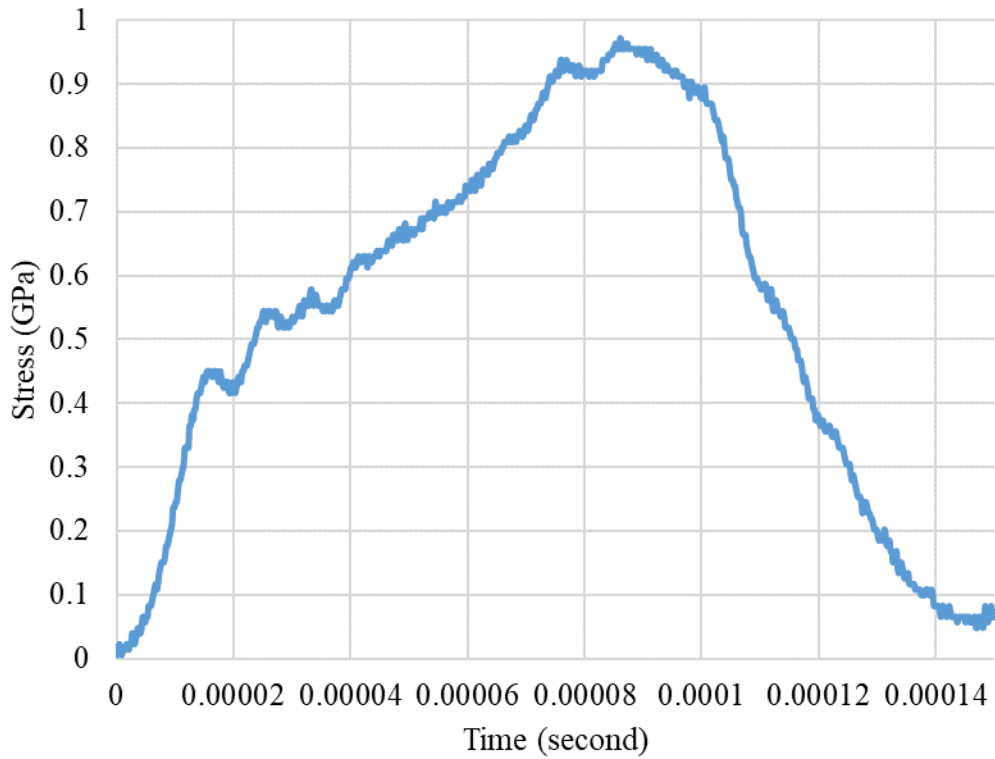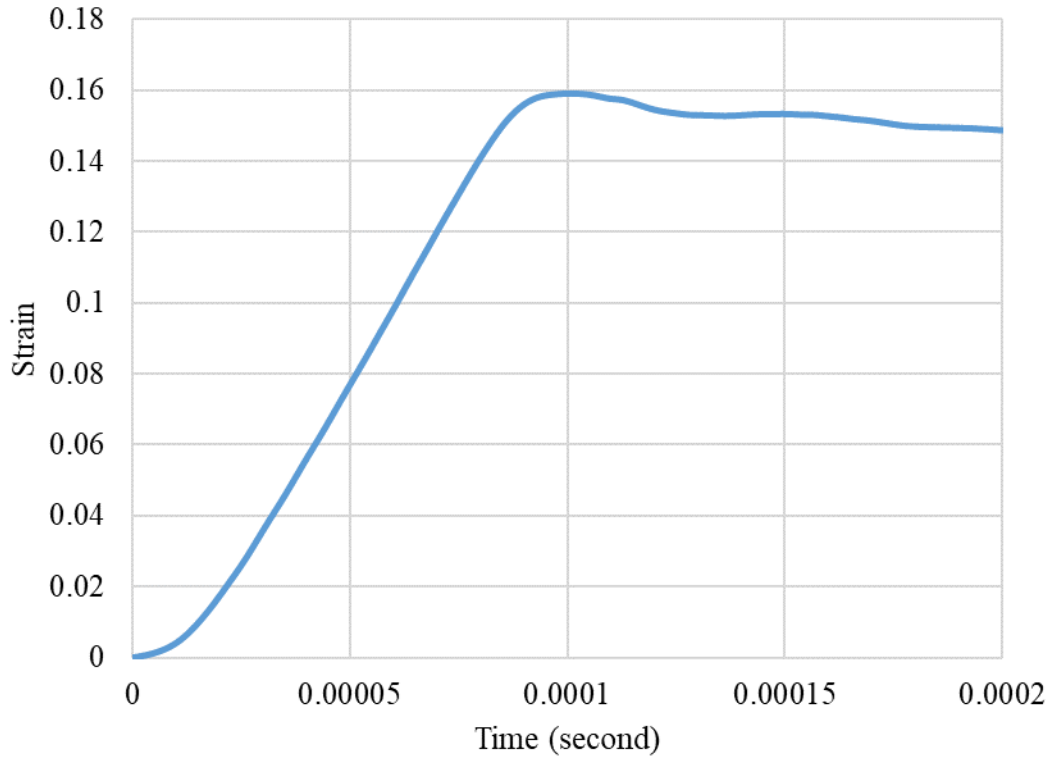
Figure A31. Aligned Test Signals

Figure A32. Sample Stress vs Time
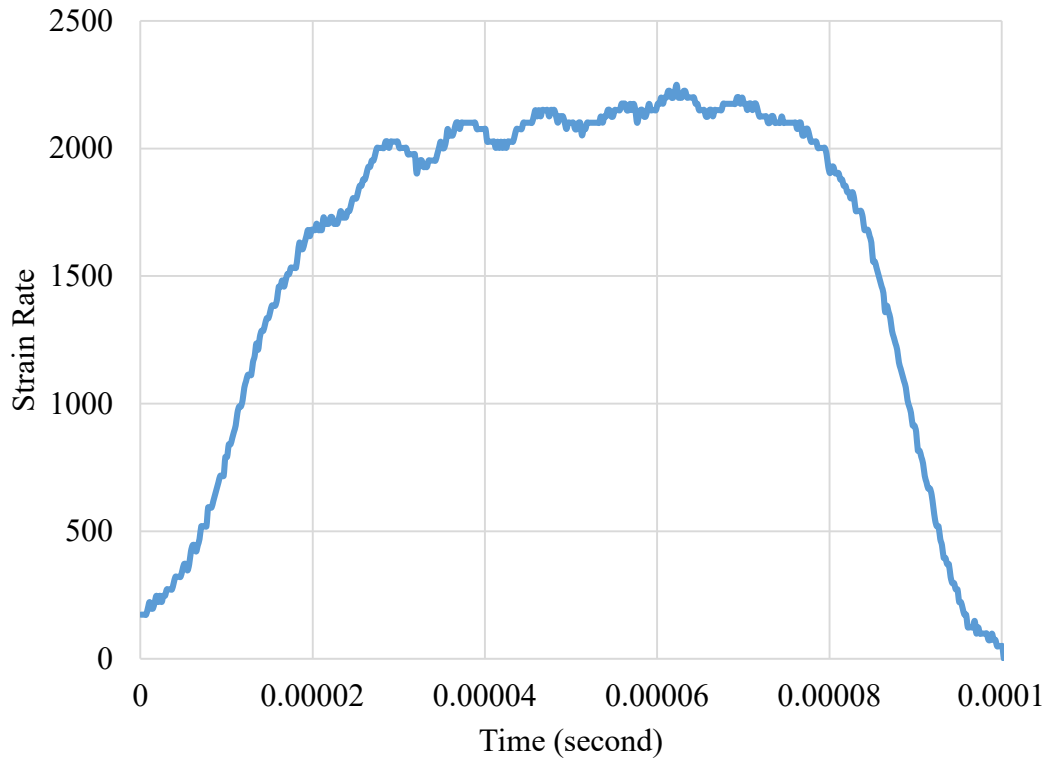
Figure A33. Sample Strain vs Time

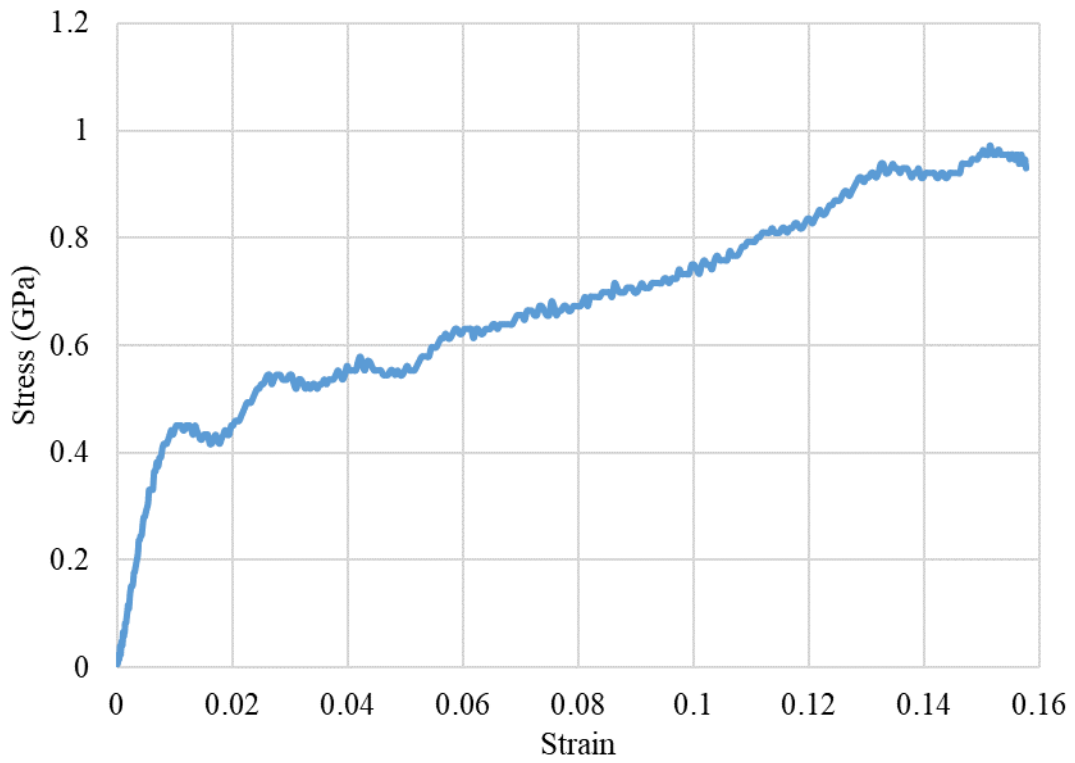**Figure A34. Sample Strain Rate vs Time**

75

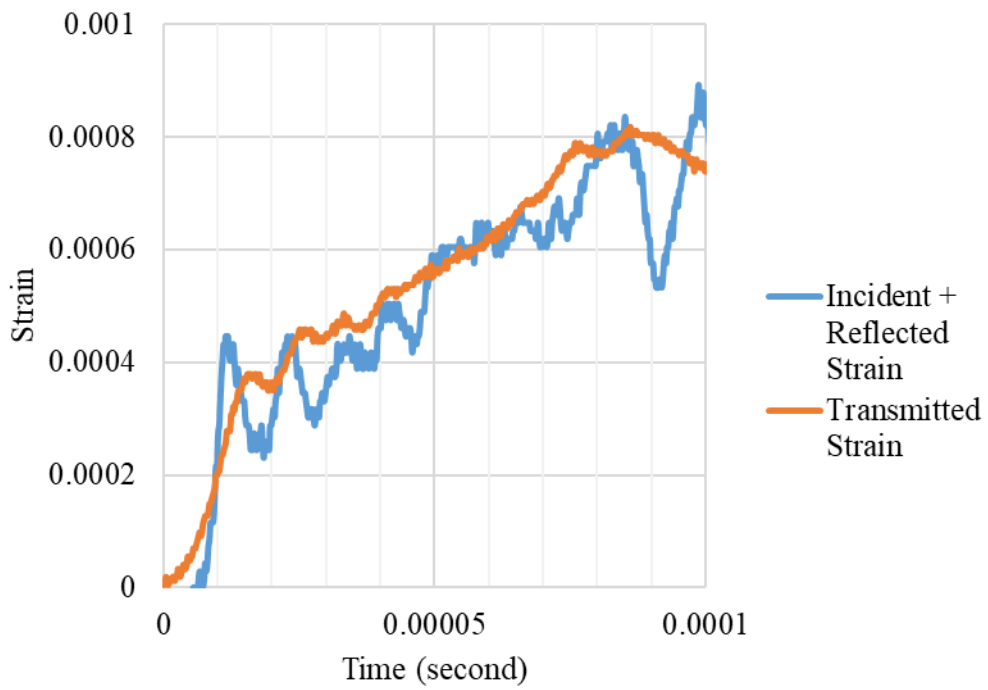**Figure A35. Sample Stress vs Strain**
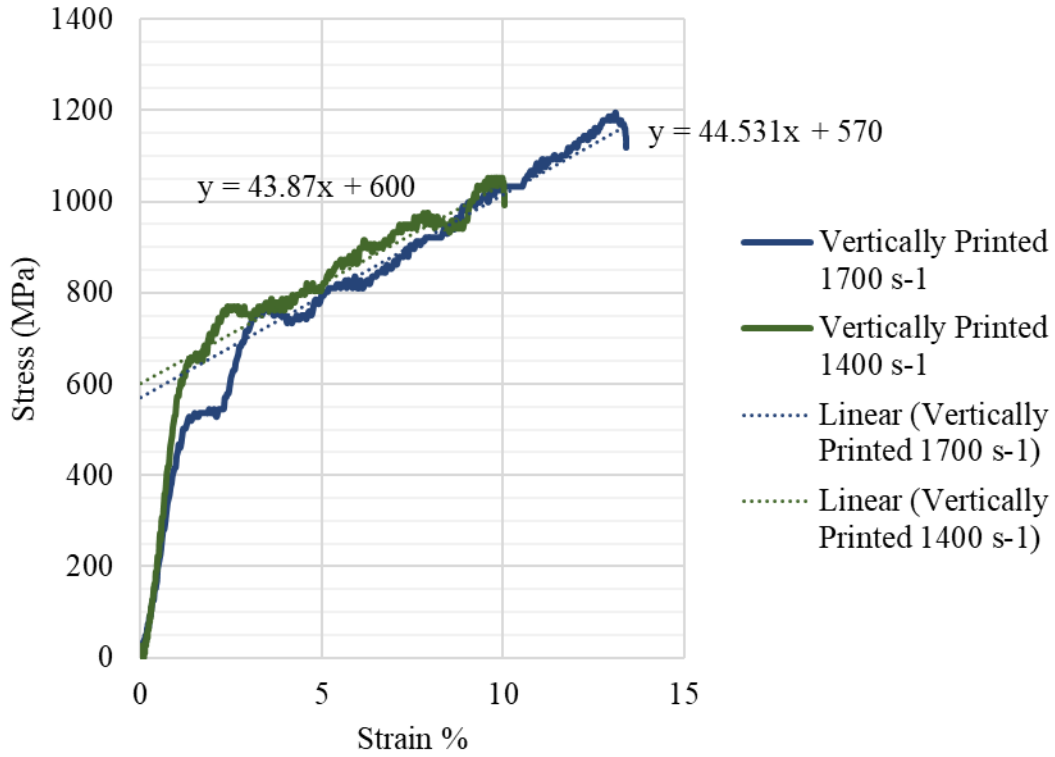

Figure A36. Sample Stress Equilibrium

Figure A37. Strain Hardening Rate for Vertically Printed Samples

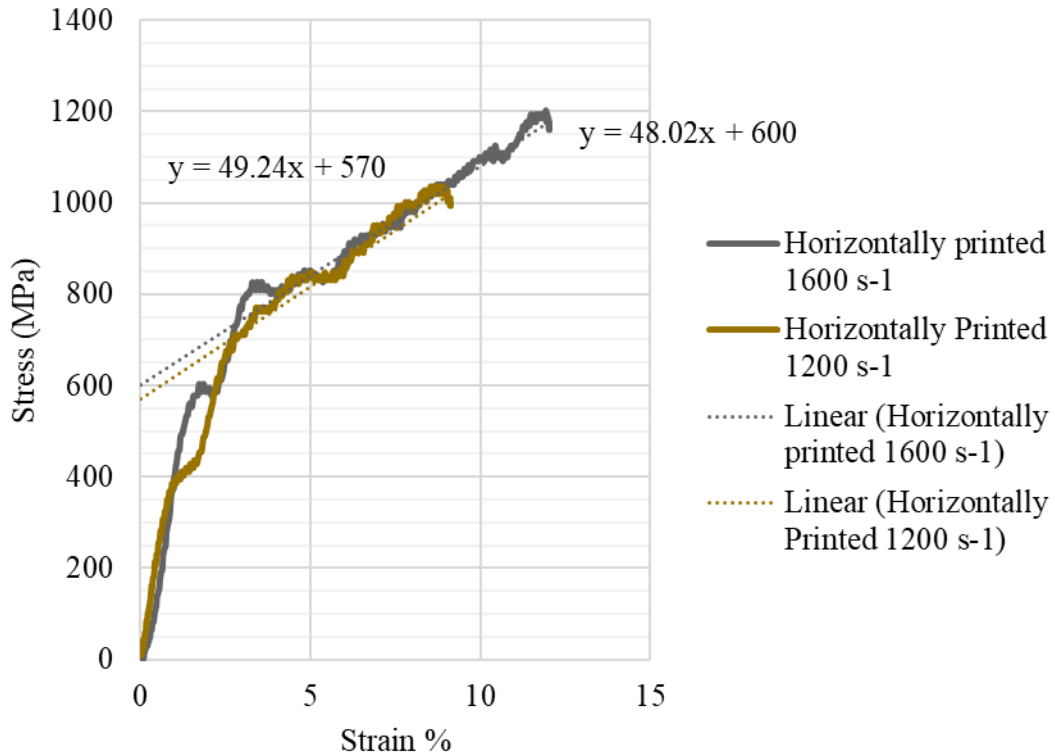**Figure A38. Strain Hardening Rate for Horizontally Printed Samples**
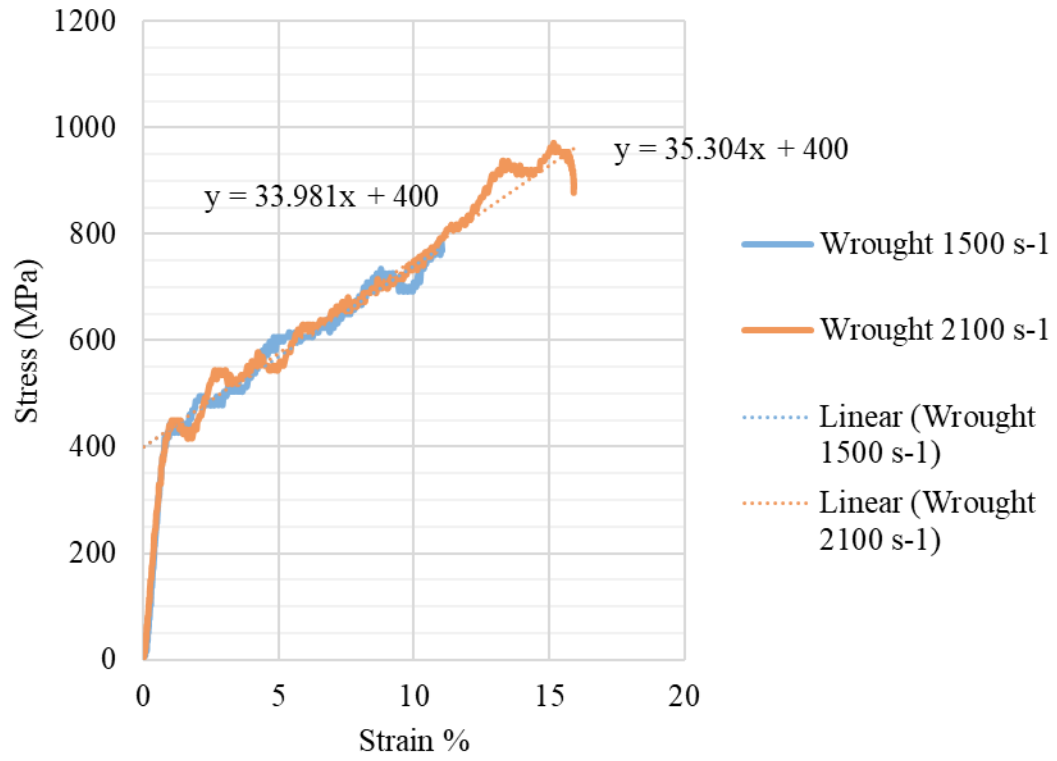
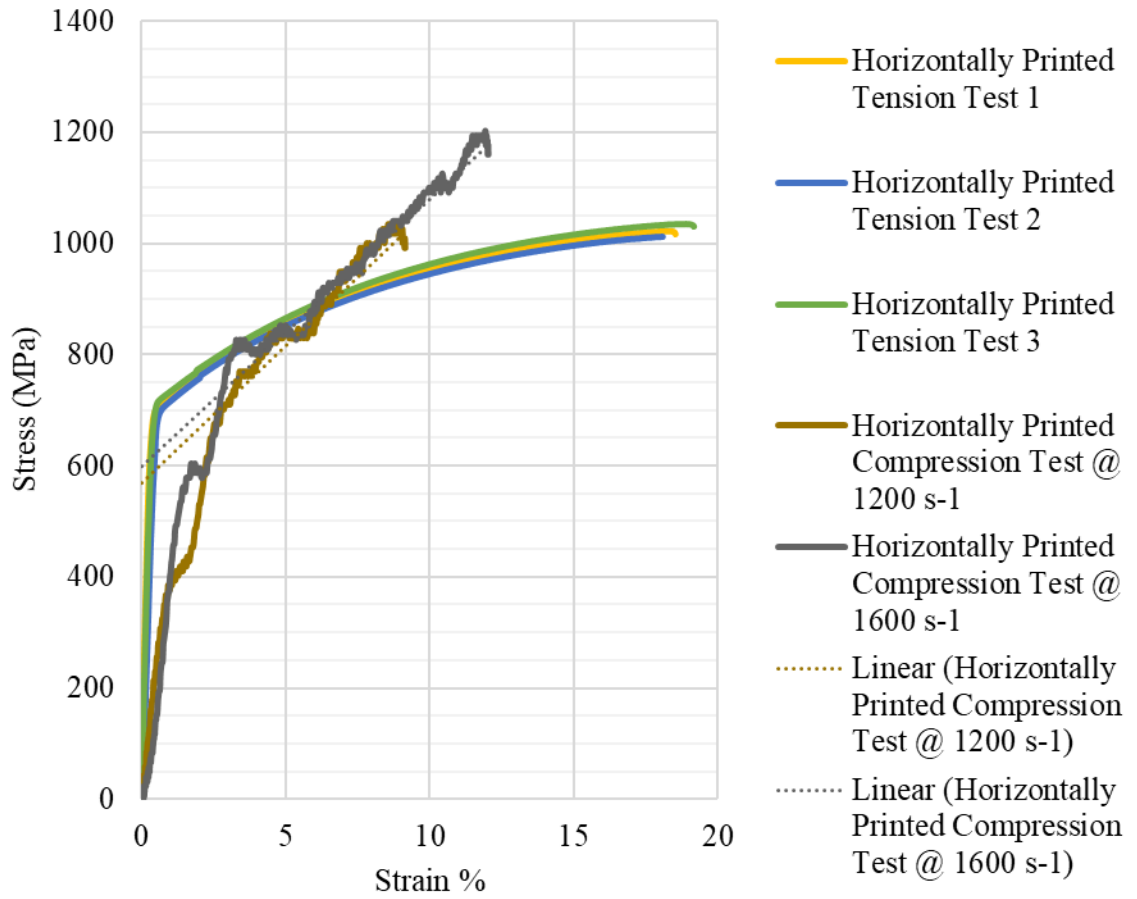**Figure A39. Strain Hardening Rate for Wrought Samples**

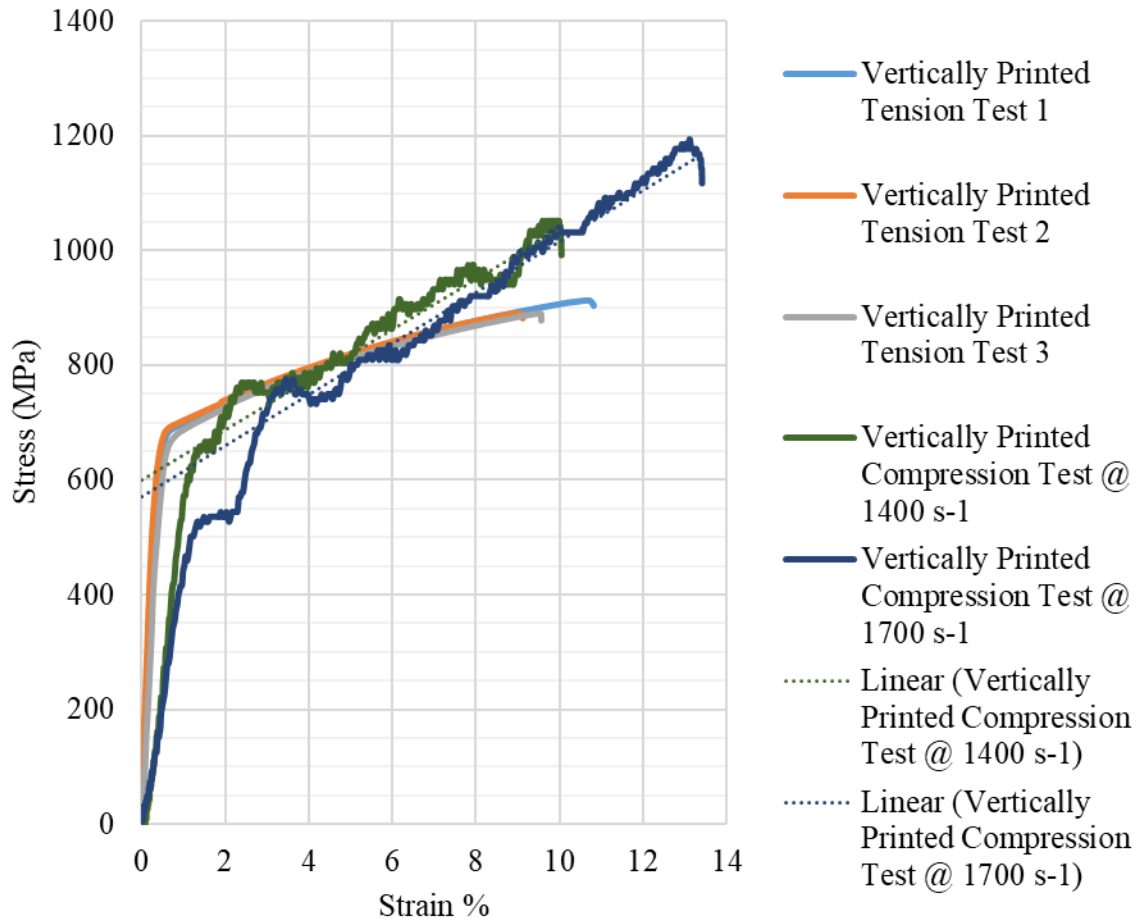**Figure A40. Comparison of Horizontally Printed Tensile and Compression Curves**

Figure A41. Comparison of Vertically Printed Tensile and Compression Curves
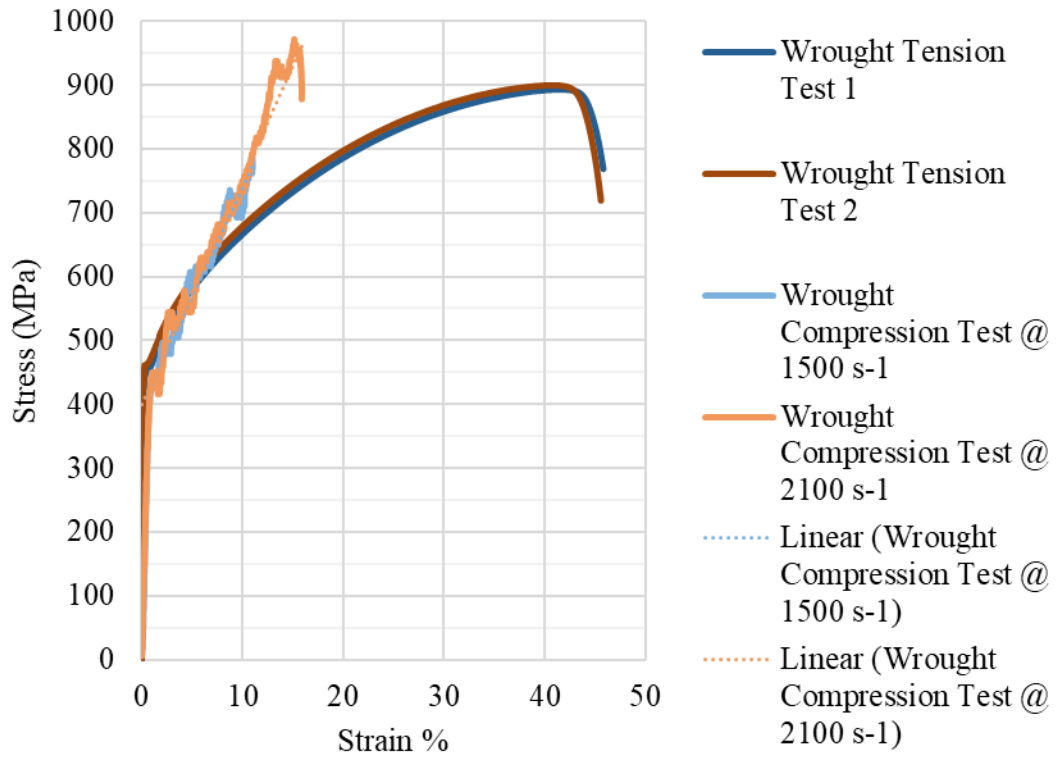
Figure A42. Comparison of Wrought Tensile and Compression Curves

Bibliography

[1]   Sharma, S., Chavan, V. M., Agrawal, R. G., Patel, R. J., Kapoor, R., and Chakravartty, J. K., 2011, "Split-Hopkinson Pressure Bar: An Experimental Technique for High Strain Rate Tests."

[2]   2000, *ASM Handbook: Mechanical Testing and Evaluation*, ASM International.

[3]   Song, B., and Chen, W., 2011, *Split Hopkinson (Kolsky) Bar: Design, Testing & Applications*, Springer.

[4]   Kolsky, H., 1949, "An Investigation of the Mechanical Properties of Materials at Very High Rates of Loading," Procedings Phys. Soc. B, **62**.

[5]   Kolsky, H., 1957, "Some Aspects of the Mechanical Testing of Nonmetallic Solids," Br. J. Appl. Phys.

[6]   Ellwood, S., Griffiths, L. J., and Parry, D. J., 1982, "Materials Testing at High Strain Rates," J. Phys. E, **15**.

[7]   Duffy, J., Campbell, J. D., and Hawley, R. H., 1971, "On the Use of a Tosional Split Hopkinson Bar to Study the Effects in 1100-0 Aluminum," J. Appl. Mech., pp. 83–91.

[8]   Frew, D., Forrestal, M. J., and Chen, W., 2002, "Pulse Shaping Techniques for Testing Brittle Materials with a Split Hopkinson Pressure Bar," Exp. Mech., **42**(1).

[9]   Frew, D. J., Forrestal, M. J., and Chen, W., 2005, "Pulse Shaping Techniques for Testing Elastic-Plastic Materials with a Split Hopkinson Pressure Bar," Exp. Mech., **45**(2).

[10] Song, B., Connelly, K., Korellis, J., Lu, W.-Y., and Antoun, B. R., 2009, "Improved Kolsky-Bar Design for Mechanical Characterization of Materials at High Strain Rates," Meas. Sci. Technol., **20**(11), p. 115701.

[11] Heard, W. F., Martin, B. E., Nie, X., Basu, P. K., and Slawson, T., 2013, "Annulus Pulse Shaping Technique for Large Diameter Kolsky Bar Characterization of Highstrength Concrete."

[12] Heard, W. F., Martin, B. E., Nie, X., Slawson, T., and Basu, P. K., 2014, "Annular Pulse Shaping Technique for Large-Diameter Kolsky Bar Experiments on Concrete," Exp. Mech., **54**(8), pp. 1343–1354.

[13] Naghdabadi, R., Ashrafi, M. J., and Arghavani, J., 2012, "Experimental and Numerical Investigation of Pulse-Shaped Split Hopkinson Pressure Bar Test," Mater. Sci. Eng. A, **539**, pp. 285–293.

[14] Zhang, Y., Wu, L., Guo, X., Kane, S., Deng, Y., Jung, Y.-G., Lee, J.-H., and Zhang, J., 2018, "Additive Manufacturing of Metallic Materials: A Review," J. Mater. Eng. Perform., **27**(1).

[15] Gonzalez, J. A., Mireles, J., Stafford, S. W., Perez, M. A., Terrazas, C. A., and Wicker, R. B., 2018, "Characterization of Inconel 625 Fabricated Using Powder-Bed-Based Additive Manufacturing Technologies," J. Mater. Process. Technol.

[16] Mutua, J., Nakata, S., Onda, T., and Chen, Z.-C., 2018, "Optimization of Selective Laser Melting Parameters and Influence of Post Heat Treatment on

Microstructure and Mechanical Properties of Maraging Steel," Mater. Des., (139), pp. 486–497.

[17] Bai, Y., Yang, Y., Wang, D., and Zhang, M., 2017, "Influence Mechanism of Parameters Process and Mechanical Properties Evolution Mechanism of Maraging Steel 300 by Selective Laser Melting," Mater. Sci. Eng. A, (703), pp. 116–123.

[18] Pleass, C., and Jothi, S., 2018, "Influence of Power Characteristics and Additive Manufacturing Process Parameters on the Microstructure and Mechanical Behavior of Inconel 625 Fabricated by Selective Laser Melting," Addtive Manuf., **24**, pp. 419–431.

[19] Li, S., Wei, Q., Shi, Y., Zhu, Z., and Zhang, D., 2015, "Microstructure Characteristics of Inconel 625 Superalloy Manufactured by Selective Laser Melting," J. Mater. Sci. Technol., **31**(9), pp. 946–952.

[20] 3-17, "LaserForm Ni625 (A) Datasheet."

[21] Li, C., White, R., Fang, X. Y., Weaver, M., and Guo, Y. B., 2017, "Microstructure Evolution Characteristics of Inconel 625 Alloy from Selective Laser Melting to Heat Treatment," Mater. Sci. Eng. A, **705**, pp. 20–31.

[22] Marchese, G., Lorusso, M., Parizia, S., Bassini, E., Lee, J.-W., Calignano, F., Manfredi, D., Terner, M., Hong, H.-U., Ugues, D., Lombardi, M., and Biamino, S., 2018, "Influence of Heat Treatments on Microstructure Evolution and Mechanical Properties of Inconel 625 Processed by Laser Powder Bed Fusion," Mater. Sci. Eng. A, **729**, pp. 64–75.

[23] 1990, *ASM Handbook: Volume 1: Properties and Selection: Irons, Steels, and High Performance Alloys*, ASM International.

[24] Lass, E. A., Stoudt, M. R., Williams, M. E., Katz, M. B., Levine, L. E., Phan, T. Q., Gnaeupel-Herold, T. H., and Ng, D. S., 2017, "Formation of the Ni3Nb δ-Phase in Stress-Relieved Inconel 625 Produced via Laser Powder-Bed Fusion Additive Manufacturing," Metall. Mater. Trans. A, **48**(11), pp. 5547–5558.

[25] Kreitcberg, A., Brailovski, V., and Turenne, S., 2017, "Effect of Heat Treatment and Hot Isostatic Pressing on the Microstructure and Mechanical Properties of Inconel 625 Alloy Processed by Laser Powder Bed Fusion," Mater. Sci. Eng. A, **689**, pp. 1–10.

[26] Donachie, M. J., and Donachie, S. James., 2002, *Superalloys: A Technical Guide*, ASM International, Materials Park, OH.

[27] Kariem, M. A., Beyon, J. H., and Ruan, D., 2012, "Misalignment Effect in the Split Hopkinson Pressure Bar Technique," Int. J. Impact Eng., **47**, pp. 60–70.